

Journal Pre-proofs

The geochemical riddle of “low-salinity gypsum” deposits

Giovanni Aloisi, Laetitia Guibourdenche, Marcello Natalicchio, Antonio Caruso, Laura Haffert, Aida El Kilany, Francesco Dela Pierre

PII: S0016-7037(22)00160-0

DOI: <https://doi.org/10.1016/j.gca.2022.03.033>

Reference: GCA 12604

To appear in: *Geochimica et Cosmochimica Acta*

Received Date: 18 October 2021

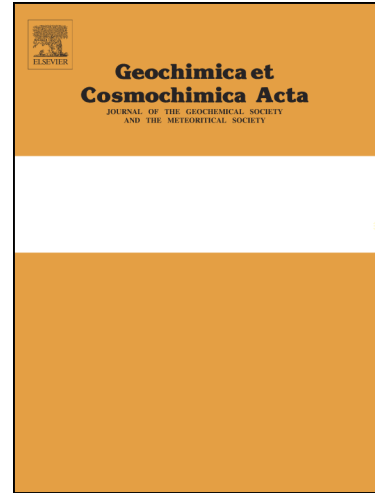
Revised Date: 19 March 2022

Accepted Date: 28 March 2022

Please cite this article as: Aloisi, G., Guibourdenche, L., Natalicchio, M., Caruso, A., Haffert, L., El Kilany, A., Dela Pierre, F., The geochemical riddle of “low-salinity gypsum” deposits, *Geochimica et Cosmochimica Acta* (2022), doi: <https://doi.org/10.1016/j.gca.2022.03.033>

This is a PDF file of an article that has undergone enhancements after acceptance, such as the addition of a cover page and metadata, and formatting for readability, but it is not yet the definitive version of record. This version will undergo additional copyediting, typesetting and review before it is published in its final form, but we are providing this version to give early visibility of the article. Please note that, during the production process, errors may be discovered which could affect the content, and all legal disclaimers that apply to the journal pertain.

© 2022 Elsevier Ltd. All rights reserved.



The geochemical riddle of “low-salinity gypsum” deposits

Giovanni Aloisi^{a,1}, Laetitia Guibourdenche^a, Marcello Natalicchio^b, Antonio Caruso^c, Laura Haffert^d, Aida El Kilany^e and Francesco Dela Pierre^b

^aUniversité de Paris, Institut de Physique du Globe de Paris, CNRS, 75005 Paris, France,
aloisi@ipgp.fr, guibourdenche@ipgp.fr

^bDipartimento di Scienze della Terra, Università di Torino, Torino, Italy,
francesco.delapierre@unito.it, marcello.natalicchio@unito.it

^cDipartimento di Scienze della Terra e del Mare, Università degli Studi di Palermo, Palermo,
Italy, antonio.caruso@unipa.it

^dGEOMAR Helmholtz-Zentrum für Ozeanforschung Kiel, Kiel, Germany,
lhaffert@geomar.de

^eSorbonne Universités, UMR 7159, LOCEAN-IPSL, Paris, France, aelkilany@yahoo.fr

¹corresponding author

Abstract

Gypsum makes up about one fifth of giant salt deposits formed by evaporation of seawater throughout Earth's history. Although thermodynamic calculations and precipitation experiments predict that gypsum precipitates when the salinity of evaporating seawater attains about 110 g kg^{-1} , gypsum deposits of the Mediterranean Salt Giant often bear the geochemical signature of precipitation from less saline water masses. Addressing this geochemical riddle is important because marine gypsum deposition and continental gypsum erosion affect the global carbon cycle. We investigated gypsum deposits formed in the marginal basins of the Mediterranean Sea during the Messinian Salinity Crisis (about 6 million years ago). These often bear low-salinity fluid inclusions and isotopically light crystallization water, confirming previous published reports that the Mediterranean Salt Giant harbors low-salinity gypsum deposits. A geochemical model constrained by fluid inclusion salinity and isotope ($^{87}\text{Sr}/^{86}\text{Sr}$, $\delta^{34}\text{S}_{\text{SO}_4}$, $\delta^{18}\text{O}_{\text{H}_2\text{O}}$, $\delta\text{D}_{\text{H}_2\text{O}}$) measurements excludes that Ca^{2+} - and SO_4^{2-} -enriched continental runoff alone provides the trigger for gypsum precipitation at low salinity. We propose that, concurrent with the prevalent evaporative conditions and with Ca^{2+} - and SO_4^{2-} -bearing runoff, the biogeochemical sulfur cycle is capable of producing a spatially-restricted and temporally-transient increase of Ca^{2+} and SO_4^{2-} within benthic microbial mats, creating local chemical conditions conductive to gypsum precipitation. This hypothesis is supported by the presence of dense packages of fossils of colorless sulfur bacteria within gypsum in several Mediterranean marginal basins, together with independent geochemical and petrographic evidence for an active biogeochemical sulfur cycle in the same basins. Should this scenario be confirmed, it would expand the range of environments that promote marine gypsum deposition; it would also imply that an additional, biological coupling between the calcium, sulfur and carbon cycles exists.

Keywords

Low-salinity gypsum, hydration water isotopes ($\delta^{18}\text{O}_{\text{H}_2\text{O}}$, $\delta\text{D}_{\text{H}_2\text{O}}$), fluid inclusions, geochemical modeling, biogeochemical S cycle

1. Introduction

Gypsum ($\text{CaSO}_4 \cdot 2\text{H}_2\text{O}$) accounts for approximately 20% of the minerals in giant salt deposits formed via the evaporation of seawater throughout Earth's history (Zharkov, 1981; Warren, 2006). Its ionic components SO_4^{2-} and Ca^{2+} are the fourth and fifth most abundant dissolved ions of seawater (Stumm and Morgan, 1996). By generating fluxes of sulfate and calcium to and from the ocean, continental gypsum weathering and marine gypsum deposition contribute in regulating ocean chemistry (Spencer and Hardie, 1990; Hardie, 1996; Hansen and Wallmann, 2003; Wortmann and Paytan, 2012; Prince et al., 2019; Turchyn and De Paolo, 2019), as well as atmosphere oxygenation, atmospheric pCO_2 and climate (Wortmann and Chernyavsky, 2007; Wortmann and Paytan, 2012; Halevy et al., 2012; Shields and Mills, 2020) on geological time scales. The study of gypsum formation in salt giants is therefore relevant to the understanding of the long-term geochemical evolution of Earth's surface.

In the sequence of minerals formed by evaporation of seawater that is often cited in textbooks (Rouchy and Blanc-Valleron, 2006; Warren, 2006; Babel and Schreiber, 2014), gypsum is the second precipitate, after carbonates and before halite. Seawater evaporation experiments (Usiglio, 1849; Valyashko, 1972; Herrmann et al., 1973) and thermodynamic solubility calculations (Van't Hoff, 1912; Stewart, 1963; Braitsch, 1971; Harvie and Weare, 1980; Harvie et al., 1980) show that, in this "classical" scenario where gypsum saturation is attained by evaporative extraction of fresh water, the point of gypsum saturation is reached when the salinity has risen to about three times the salinity of modern ocean water ($\sim 110 \text{ g kg}^{-1}$). This salinity threshold is the same in: (i) closed systems where the only water flux is evaporative loss; (ii) constant-volume systems where the water lost by evaporation is replenished by influx from the ocean; and (iii) open systems with leakage, where, in addition to evaporative loss and influx from the ocean, brine is lost to the ocean via a density-driven counter flux (Sanford and Wood, 1991). In summary, in evaporitic systems where the evaporating fluid is seawater (marine evaporites) (Hardie, 1984), gypsum deposition is expected to start at a salinity of $\sim 110 \text{ g kg}^{-1}$ and proceed until the beginning of the precipitation of halite ($\sim 320 \text{ g kg}^{-1}$) (Harvie et al., 1980).

Geochemical evidence from gypsum contained in the Mediterranean Salt Giant suggests that this scenario is not always true. The Mediterranean Salt Giant is Earth's most recent giant salt deposit (Ryan, 2009; Roveri et al., 2014); it formed between 5.97 and 5.33 Ma at the end of the Messinian age of the Miocene epoch, when the Mediterranean Sea underwent an extreme environmental change known as the Messinian Salinity Crisis (Hsü et al., 1973; Ryan, 2009;

Roveri et al., 2014). During this event, a huge salinity increase led to the deposition of a salt-dominated sedimentary body that occupies a volume of 1 million km³ (Haq et al., 2020). Mediterranean Salt Giant-related deposits are found both in the offshore deep Mediterranean basin (Haq et al., 2020) and in onshore intermediate-to-shallow marginal Mediterranean basins (Lugli et al., 2010; Roveri et al., 2014) (Fig. 1). The geochemical signature of gypsum deposited in some marginal basins (Natalicchio et al., 2014; Evans et al., 2015; Costanzo et al., 2019) suggest its formation from water masses with a salinity much lower than that (~110 g kg⁻¹) predicted by evaporation experiments (Usiglio, 1849; Valyashko, 1972; Herrmann et al., 1973) and thermodynamic models (Van't Hoff, 1912; Stewart, 1963; Braitsch, 1971; Harvie and Weare, 1980; Harvie et al., 1980). In this paper, we will refer to this geochemically peculiar gypsum as “low-salinity gypsum”.

Evidence for low-salinity gypsum in the Messinian Salinity Crisis comes primarily from the study of gypsum primary fluid inclusions. These suggest average salinities of gypsum parent waters equal to 16 g kg⁻¹ in the Piedmont Basin (northern Italy) (Natalicchio et al., 2014), 32 g kg⁻¹ in the Sorbas basin (Spain) (Evans et al., 2015) and 27 g kg⁻¹ in the Catanzaro Trough (southern Italy) (Costanzo et al., 2019). These values are between 14 % and 29 % of the threshold salinity at which gypsum precipitates from evaporating seawater in the “classical” scenario cited above. The absence of evidence for recrystallisation of the primary gypsum deposits at both macro- and microscopic scale (Natalicchio et al., 2014; Costanzo et al., 2019) suggests that the low salinity signature is pristine and not the result of a diagenetic overprint. These data question the purely evaporitic origin of the Mediterranean gypsum deposits: if not exclusively evaporation of seawater, what process concentrated - or contributed to concentrate - dissolved Ca²⁺ and SO₄²⁻ to the point of gypsum saturation?

Deviations from the purely marine evaporitic mineral sequence can take place if the source of evaporating fluid is different from seawater (Hardie, 1984). In the case of the Messinian Salinity Crisis, there is ample geochemical evidence from Sr-isotopes that continental runoff contributed significant volumes of freshwater to the Mediterranean Sea during gypsum deposition (Topper et al., 2011). Supported by these observations, two hypotheses point to high dissolved Ca²⁺ and SO₄²⁻ in a fresh or brackish water source as the trigger for the formation of low-salinity gypsum during the Messinian Salinity Crisis. The first hypothesis involves the leaching of exposed penecontemporaneous Messinian gypsum (Natalicchio et al., 2014; Evans et al., 2015) - with the possible addition of Ca²⁺ and SO₄²⁻ from carbonate and pyrite weathering (Berner and Berner, 2012) - and the re-precipitation in an adjacent marginal

basin. The second hypothesis involves input into the Mediterranean of water via the Paratethys (Grothe et al., 2020); this idea relies on the salinity and chemical composition of the modern Caspian Sea that is brackish (salinity $\sim 12 \text{ g kg}^{-1}$ compared to a seawater salinity $\sim 35 \text{ g kg}^{-1}$) but has dissolved Ca^{2+} ($\sim 8 \text{ mmol kg}^{-1}$) and SO_4^{2-} ($\sim 31 \text{ mmol kg}^{-1}$) concentrations comparable to those of the modern ocean (Clauer et al., 2000). Both these hypotheses remain unevaluated.

Here we present new geochemical data in support of the formation of Mediterranean marginal gypsum deposits from low-salinity ($< 110 \text{ g kg}^{-1}$) water masses. We expand the observations of Natalicchio et al. (2014), Evans et al. (2015) and Costanzo et al. (2019) to include novel fluid inclusion salinity data from primary gypsum deposits of the Vena del Gesso basin (northern Italy) and the isotope composition of primary gypsum hydration water ($\delta^{18}\text{O}_{\text{H}_2\text{O}}$ and $\delta\text{D}_{\text{H}_2\text{O}}$) from the Caltanissetta basin (Sicily), the Vena del Gesso basin and the Piedmont basin (northern Italy), as well as the hydration water isotope ($\delta^{18}\text{O}_{\text{H}_2\text{O}}$ and $\delta\text{D}_{\text{H}_2\text{O}}$) composition from secondary gypsum from the Volterra basin. Gypsum crystallization water isotopes are complementary to fluid inclusion salinity measurements, since gypsum crystallization water pervades the whole crystalline lattice, rather than being concentrated in spatially distinct portions of the crystal matrix. In addition, we present the isotope composition of sulfur ($\delta^{34}\text{S}_{\text{SO}_4}$) and oxygen ($\delta^{18}\text{O}_{\text{SO}_4}$) of the sulfate ion in gypsum from the Caltanissetta, the Vena del Gesso and Piedmont basins, that provide information on sulfate sources and the biogeochemical sulfur cycle.

We apply a simple geochemical model that simulates the evolution of salinity, gypsum saturation state and water isotope composition ($\delta^{18}\text{O}$ and δD) during the evaporation of mixtures of seawater and a Ca^{2+} and/or SO_4^{2-} -bearing freshwater source. The model is used to (i) evaluate the potential of gypsum hydration water isotopes as indicators of the formation of gypsum from low-salinity parent waters, and (ii) evaluate scenarios for low-salinity gypsum formation that involve a Ca^{2+} and SO_4^{2-} -rich fresh water source. Finally, we discuss a complementary scenario for the formation of low-salinity gypsum that involves the spatially-restricted and temporally-transient increase of Ca^{2+} and SO_4^{2-} at the sediment-water interface of the basin triggered by the biogeochemical sulfur cycle.

2. Geological setting, study areas and gypsum lithofacies

2.1 Geological setting of Mediterranean Salt Giant deposits

The bulk of the evaporitic deposits that make up the Mediterranean Salt Giant (primarily halite and gypsum, with subordinate K-Mg salts such as kainite, carnallite and bishofite) were deposited in the deep Mediterranean basin where they are buried under several hundreds of meters of Plio-Quaternary pelagic sediments (Roveri et al., 2014; Haq et al., 2020).

Evaporites (mainly gypsum, with minor halite and K-Mg salts) were also deposited in intermediate- (1000 to 200 m) to shallow- (< 200 m) depth marginal basins, now mostly exposed on land (Lugli et al., 2010; Dela Pierre et al., 2014) (Fig. 1). Marginal basin deposits have been extensively studied (Krijgsman et al., 1999, 2002; Rouchy and Caruso, 2006; Lugli et al., 2010; Dela Pierre et al., 2011; Manzi et al., 2012, 2013, 2016; Roveri et al., 2014, 2019; Cosentino et al., 2018). They form gypsum-dominated sedimentary bodies that can be followed for tens of kilometers both onshore and in the marginal offshore domain (Driussi et al., 2015; Ochoa et al., 2015; Raad et al., 2020; Manzi et al., 2020).

Astronomical dating of marginal onshore successions across the Mediterranean has shown that the onset of the Messinian Salinity Crisis is a synchronous event at 5.97 Ma (Krijgsman et al., 1999; Manzi et al., 2013) or slightly diachronous (Rouchy and Caruso, 2006; Caruso et al., 2015). Messinian evaporites were originally subdivided into two informal stratigraphic units: Lower Evaporites, including gypsum and the thick massive halite and K-Mg salts of Sicily and deep basins, and Upper Evaporites, mostly consisting of gypsum (Rouchy and Caruso, 2006 and references therein). More recently a different terminology was proposed following the three-stage model of the Messinian Salinity Crisis events that is based on outcrop studies of key section from different Mediterranean sub-basin (CIESM, 2008; Roveri et al., 2014). According to this model, whose validity in the entire Mediterranean basin is debated (Meijlison et al., 2019; Artiaga et al., 2021), up to 16 precession-controlled shale-gypsum cycles, known as the Primary Lower Gypsum, were deposited in silled marginal basins during the first phase of the Messinian Salinity Crisis (5.97-5.60 Ma). During the second phase of the Messinian Salinity Crisis (5.60-5.55 Ma), the Primary Lower Gypsum deposits were uplifted and partially eroded, resulting in clastic gypsum deposits (Resedimented Lower Gypsum unit) that locally interfinger (Caltanissetta basin) with halite and K-Mg salts (Manzi et al., 2021). Primary gypsum deposition took place again in the southern (Caltanissetta basin) and eastern (Cyprus, Crete) Mediterranean marginal basins in the third phase of the Messinian Salinity Crisis (5.55 – 5.33 Ma) forming the Upper Gypsum unit (corresponding to the Upper Evaporites) that consist of up to 8 marl/gypsum cycles

(Roveri et al., 2014). The third phase of the Messinian Salinity Crisis also contains a non-evaporitic, brackish water deposit called Lago-Mare (Andreetto et al., 2021) that preceded the reconnection of the Mediterranean with the Atlantic Ocean at the Miocene-Pliocene boundary (5.33 Ma).

2.2 Study areas

We investigated onshore Primary Lower Gypsum and Upper Gypsum deposits from the Caltanissetta basin: Santa Elisabetta section ($37^{\circ}26'50''N$, $13^{\circ}32'58''E$; 14 samples), Gibliscemi section ($37^{\circ}12'21''N$, $14^{\circ}16'16''E$; 6 samples) and Eraclea Minoa section ($37^{\circ}23'37''N$, $13^{\circ}17'28''E$; 32 samples); Primary Lower Gypsum deposits from the Vena del Gesso basin: Monticino section ($44^{\circ}13'29''N$, $11^{\circ}45'43''E$; 40 samples) and Monte Tondo quarry section ($44^{\circ}15'04''N$, $11^{\circ}40'13''E$; 5 samples); Primary Lower Gypsum deposits from the Piedmont basin: Banengo section ($45^{\circ}04'18.5''N$ $8^{\circ}03'25.2''E$; 45 samples), Arnulfi section ($43^{\circ}37'06''N$; $7^{\circ}53'41''E$; 27 samples) and Pollenzo section ($44^{\circ}41'08''N$; $7^{\circ}55'33''E$; 71 samples) (Fig. 1b). Next to these primary gypsum precipitates, we analyzed Primary Lower Gypsum deposits from the Castellina Quarry ($45^{\circ}25'14''N$; $10^{\circ}32'55''E$; 6 samples) of the Volterra basin (Tuscany, Italy) that are evidently secondary deposits based on their macroscopic features. A description of the above-mentioned marginal basins and of the investigated lithological sections is provided in the Supplementary Material section. The investigated stratigraphic sections are presented in Fig. 1b.

2.3 Gypsum lithofacies

The Primary Lower Gypsum and Upper Gypsum units comprise different gypsum lithofacies that are described below. The names of lithofacies presented in italics in this section are used to describe the samples included in this study and listed in the sample tables S1 to S8.

Selenite gypsum

In the Vena del Gesso and Piedmont basins, the lower beds of the Primary Lower Gypsum unit are up to 30 m thick and consist of vertically-oriented, twinned (arrow head and swallow tail), selenite crystals (Orti, 2011) nucleated and grown on the basin floor (hereafter, bottom-grown); they form the *massive* and *banded selenite* lithofacies. The *massive selenite* is composed of dm-sized crystals with uniform size throughout the beds. Crystals up to 2.5 m high (giant selenite) are locally observed; the *banded selenite* is composed of cm-sized palisades of twinned crystals that are separated by mm-thick clay and carbonate layers. In both the *massive* and the *banded selenite* lithofacies, the re-entrant angle of the crystals shows an

internal lamination produced by the alternation of turbid laminae, rich in solid inclusions (mostly filamentous microfossils and clay-rich floccules), and limpid laminae in which solid inclusions are scarce or absent. Such lamination reflects the influence of short-term (annual, seasonal) climate variability (Orti, 2011; Dela Pierre et al., 2015; Reghizzi et al., 2018). The 6th gypsum bed and the overlying beds are characterized by the presence of the *branching selenite* lithofacies, composed of cm-sized horizontally-oriented crystals grouped together to form asymmetrical conical structures with one side (branch) more developed than the other (Lugli et al., 2010; Natalicchio et al., 2021). In the Vena del Gesso basin, *branching selenite*, also bottom-grown, is found in the upper part of the gypsum beds, above the *massive* and *banded selenite* lithofacies (Lugli et al., 2010). The *massive selenite* lithofacies is present also in the Caltanissetta basin where it forms the bulk of gypsum deposits in the Santa Elisabetta section (Primary Lower Gypsum), the upper part of the Gibliscemi section and the Eraclea Minoa section (Upper Gypsum)

Laminar gypsum

This latter lithofacies, formerly termed *balatino* (Ogniben, 1957), consists of the alternation of gypsum rich laminae (1-2 mm thick) and clay and dolomite-rich laminae (100-200 µm thick). The gypsum-rich laminae are composed of interlocked prismatic and acicular crystals ranging in size from a few µm to some hundreds of µm. The *laminar* gypsum represents an *in-situ* cumulate deposit, formed by the nucleation of tiny gypsum crystal in the water column and their subsequent deposition on the seafloor (Natalicchio et al., 2021). In the Piedmont basins, the *laminar* gypsum is associated to the *branching selenite* facies (Natalicchio et al., 2021). In sections from the Caltanissetta basin considered in this work, *laminar* gypsum occurs in the Gibliscemi section and in the Eraclea Minoa section (Upper Gypsum).

Secondary gypsum lithofacies

Following episodes of dehydration-hydration, gypsum is transformed into anhydrite, and anhydrite is subsequently transformed into gypsum (see supplementary material), with a complete loss of the original gypsum lithofacies. The neo-formed gypsum lithofacies include: *alabastrine* gypsum (an aggregate of gypsum microcrystals), *fibrous* gypsum (fracture-filling fibrous gypsum crystals) and *chicken-wire* gypsum (microcrystalline gypsum nodules separated by thin seams of host sediments). In our study, these secondary gypsum lithofacies occur only in the Volterra basin (Testa and Lugli, 2000).

3. Methods

In this section we present a summary of the analytical methods used. A full description of the methods is provided in the Supplementary Materials section.

3.1 Sampling

Samples were obtained from the outcrop by mechanically breaking gypsum fragments with a geological hammer. Care was taken to remove a few centimeters of the gypsum surface to avoid sampling the weathered surface layer. A few core samples from the Santa Elisabetta and Gibliscemi sections were obtained using a water-cooled drill with a core-bit diameter of 3 cm. This sampling technique was not used further because it is time-consuming, has the potential of heating the gypsum and did not result in gypsum samples that were visually more pristine than those obtained with the geological hammer. Sample tables are presented in the Supplementary Materials section. Sampling positions appear in Fig 1b.

3.2 Isotopic composition of gypsum hydration water

Gypsum hydration water was extracted following the protocol of Fontes (1966) (see supplementary methods). Liquid water samples obtained by dehydrating gypsum were analyzed for oxygen ($\delta^{18}\text{O}$) and hydrogen (δD) isotope composition using a Picarro L2130-i (LOCEAN laboratory, Sorbonne Université) or a Picarro L2140-i (IPGP, Université de Paris) laser spectrometers. The isotope composition of gypsum hydration water is expressed in delta notation ($\delta^{18}\text{O}$ for oxygen 18 and δD for deuterium) defined as the per mil deviation of the $^{18}\text{O}/^{16}\text{O}$ and D/H ratios in the seawater from the ratio in the Vienna Standard Mean Ocean Water (VSMOW). The standard deviation of the isotope values of multiple analyses of the same gypsum hydration water sample are typically smaller than 0.05 ‰ for $\delta^{18}\text{O}$ and 0.2 ‰ for δD .

3.3 Isotopic composition of the sulfate ion of gypsum

Gypsum samples were ground and dissolved in deionized and acidified water. The solution was then filtered (0.8 µm), heated and the dissolved sulfate was precipitated as barium sulfate by addition of a 1 N-BaCl₂ solution. The precipitated BaSO₄ was filtered (0.8 µm), washed with deionized water and dried in an oven at 90 °C.

The $\delta^{34}\text{S}$ and $\delta^{18}\text{O}_{\text{SO}_4}$ of gypsum sulfate from the Piedmont and Caltanissetta basins were measured at the LOCEAN laboratory, Sorbonne Université. Isotope analyses were carried out in triplicate on a Thermo Scientific Delta V Advantage IRMS on CO ($\delta^{18}\text{O}$) and SO₂ ($\delta^{34}\text{S}$) produced respectively by pyrolysis (using a Conflo IV interface, on 150 µg of barium

sulphate plus 1 mg of AgCl) and combustion (using a Flash-EA2000 Thermal Conversion Elemental Analyzer unit, on 250 µg of barium sulfate plus 1 mg of V₂O₅) of BaSO₄ obtained by chemical precipitation of sulfate gypsum in a BaCl solution. The δ¹⁸O and δ³⁴S values were calibrated using the IAEA international reference NBS 127 ($\delta^{18}\text{O} = +8.59 \pm 0.2\text{\textperthousand}$ vs SMOW and $\delta^{34}\text{S} = +21.12 \pm 0.22\text{\textperthousand}$ vs CDT (Brand et al., 2014)).

The δ¹⁸O_{SO4} of gypsum sulfate from the Vena del Gesso basin was measured at the Université de Bourgogne (Dijon) on purified barite samples obtained with the procedure described above. Isotope measurements were carried out in duplicate on an Elementar vario PYRO cube elemental analyzer in-line with an Isoprime 100 mass spectrometer in continuous flow mode. Analytical errors are ±0.4‰ (2σ) based on replicate analyses (n = 21) of the international barite standard NBS-127, which was used for data correction via standard-sample-standard bracketing.

δ³⁴S_{SO4} of gypsum sulfate from the Vena del Gesso basin was measured at IPGP (Paris) on gaseous SF₆ with a MAT-253 dual inlet mass spectrometer. The gypsum powder was first reduced with a “Thode” solution into H₂S (Thode et al., 1961) that was subsequently trapped in NaOH solution and then precipitated into Ag₂S by adding a AgNO₃ solution (Geng et al., 2018). The entire extraction procedure gave sulfur yields between 76 and 116% (n=29) with a mean of 95±2% (1σ), with the lowest yields explained by higher amount of non-sulfur bearing mineral phases such as clays. Ag₂S was then introduced into Ni reaction bombs, reacted with F₂ at 310°C overnight to produce SF₆ and then purified cryogenically and by gas chromatography (Ono et al., 2006; Labidi et al., 2012). The SF₆ was then introduced into the MAT-253 for isotopic measurements that yielded analytical precisions of 0.2‰ (accounting for full reproducibility of the steps described above). Sulfur and oxygen isotope data are expressed in delta notation defined as the per mil deviation of the ³⁴S/³²S and ¹⁸O/¹⁶O ratios from the international CDT and SMOW standards. The analytical precision is ±0.1‰ and ±0.2‰ for δ³⁴S and δ¹⁸O measurements respectively.

3.4 Salinity of gypsum fluid inclusions

Primary fluid inclusions were studied from 6 bottom-grown gypsum samples from the Monte Tondo section (Vena del Gesso basin). A total of 60 microthermometric measurements were carried out using a calibrated Linkam THMSG600 heating–freezing stage attached to an Olympus polarizing microscope using the method described in Natalicchio et al. (2014) and explained in the Supplementary Materials section. For each analyzed sample, several micro-

samples (fragments) from the re-entrant angle of gypsum twins were investigated for their fluid inclusions. Salinities of the fluid inclusions were calculated from the final melting temperatures of ice and expressed as weight % NaCl equivalent (Bodnar, 1993) and as ppt of seawater (Goldstein and Reynolds, 1994). Petrographic and cathodoluminescence observations were carried out by plane-polarized and cross-polarized light microscopy using a CITL 8200 mk3 equipment, operating at about 17 kV and 400 μ A.

3.5 Mixing-evaporation model

We used a numerical model to simulate the evolution of salinity and isotope composition ($\delta^{18}\text{O}_{\text{H}_2\text{O}}$, $\delta\text{D}_{\text{H}_2\text{O}}$, $^{87}\text{Sr}/^{86}\text{Sr}$ and $\delta^{34}\text{S}_{\text{SO}_4}$) of mixtures of Atlantic Ocean water and freshwater from continental runoff subject to evaporation until the point of gypsum saturation ($\Omega_{\text{Gypsum}} = 1$). The model is a simple mixing-evaporation model in which the mixing and evaporation processes are considered successively, rather than contemporaneously, and where the compositional change in time is produced exclusively by the decrease of the total amount of water in the system. The continental runoff endmember can be ion-free or can contain dissolved Ca^{2+} and SO_4^{2-} , reflecting the addition of these ions via gypsum, carbonate and pyrite weathering. The model considers initial fluid mixtures that have dissolved $\text{Ca}^{2+}/\text{Cl}^-$ and $\text{SO}_4^{2-}/\text{Cl}^-$ ratios ranging from those of seawater (0.0188 and 0.052, respectively) to ratios ten times larger, while the other ion/ Cl^- ratios are held equal to those of seawater. The model calculates the saturation state with respect to gypsum as a function of water temperature (5–35°C), ionic strength and Ca^{2+} and SO_4^{2-} concentration by using an interpolation function based on the results of Pitzer ion-interaction calculations that include all major ions of seawater and are designed to cover all the chemical compositions explored with the evaporation model. Although carbonate alkalinity (dissolved HCO_3^- and CO_3^{2-}) is included in the Pitzer system, to simplify the evaporation model we do not consider precipitation of carbonate minerals in our simulations. This simplification has only small effects on model results since only ~ 1 mM of dissolved Ca^{2+} would be sequestered by seawater dissolved total alkalinity (~ 2 mM) prior to reaching gypsum saturation. The isotope composition ($\delta^{18}\text{O}_{\text{H}_2\text{O}}$, $\delta\text{D}_{\text{H}_2\text{O}}$, $^{87}\text{Sr}/^{86}\text{Sr}$ and $\delta^{34}\text{S}_{\text{SO}_4}$) of gypsum samples from the Primary Lower Gypsum and Upper Gypsum units discussed in the present work is used, in conjunction with the model, to evaluate existing scenarios for the formation of low-salinity gypsum deposits. The model is compiled in the software Wolfram Mathematica 12 and is run on an Apple iMac desktop computer. A full description of the mixing-evaporation model and the Pitzer model are provided in the supplementary materials section.

4. Analytical results

A total of 60 new fluid inclusion salinity measurements were obtained from 6 samples of vertically oriented selenite crystals from the Primary Lower Gypsum unit of the Vena del Gesso basin (Primary Lower Gypsum cycles 3, 4, 6, 10, 14) (Supplementary Table 9). The salinity of single fluid inclusion varies from 5.5 to 179 g kg⁻¹ (Fig. 2a). The large range of salinities measured within the same sample is related to primary fluid inclusions belonging to different growth bands, likely suggesting salinity fluctuations during gypsum growth. The average salinity of the 6 samples varies from 24.5 to 78.2 g kg⁻¹, while the average of all salinity measurements is equal to 52.2 g kg⁻¹. Compared to the average fluid inclusion salinity data from Primary Lower Gypsum unit of the Piedmont basin (16 g kg⁻¹, Natalicchio et al., 2014), the Upper Gypsum unit of the Catanzaro Trough (27 g kg⁻¹; Costanzo et al., 2019) and the Primary Lower Gypsum unit of the Sorbas basin (32.3 g kg⁻¹; Evans et al., 2015), the Vena del Gesso basin Primary Lower Gypsum fluid inclusions are more saline (Table 1).

We calculated the isotope composition of gypsum parent waters from the measured isotope composition of gypsum hydration water, using the water-gypsum oxygen and hydrogen fractionation factors determined by Gazquez et al. (2017) ($\alpha^{18}\text{O}_{\text{GYP-H}_2\text{O}} = 1.0035$; $\alpha\text{D}_{\text{GYP-H}_2\text{O}} = 0.9821$ at 20°C). The gypsum parent waters from the eight newly investigated sections define linear trends in the $\delta^{18}\text{O}$ - δD space (Fig 2b, c and d). In the Caltanissetta basin, the range of $\delta^{18}\text{O}$ and δD values (-2.62 < $\delta^{18}\text{O}$ ‰ vs SMOW < 5.78; -22.44 < δD ‰ vs SMOW < 28.05) extends from values approaching those of modern Mediterranean Sea salt works (Fontes, 1966; Fontes and Gonfiantini, 1967; Longinelli, 1979; Evans et al., 2015), to values 3.6 ‰ lighter than Atlantic waters in front of Gibraltar (Benetti et al., 2017a). In the Piedmont basin, the gypsum parent waters are markedly lighter (-7.0 < $\delta^{18}\text{O}$ ‰ vs SMOW < 3.15; -56.43 < δD ‰ vs SMOW < 23.48) than those from the Caltanissetta basin, while the Vena del Gesso basin parent waters (0.99 < $\delta^{18}\text{O}$ ‰ vs SMOW < 4.34; 0.91 < δD ‰ vs SMOW < 22.07) are isotopically intermediate between those of the Caltanissetta and the Piedmont basins. Compared to the new data presented here, gypsum parent waters from Primary Lower Gypsum cycle 6 in the Sorbas basin (-2.06 < $\delta^{18}\text{O}$ ‰ vs SMOW < 3.21; -17.04 < δD ‰ vs SMOW < 15.03) (Fig. 2e; Evans et al., 2015) are intermediate between those of the Vena del Gesso and the Piedmont basins. Except from the two massive selenite samples that have similar isotopic values than gypsum from the Piedmont basin, the parent waters of alabastrine, fibrous and chicken-wire gypsum samples from the Castellina Marittima Quarry in the

Volterra basin show the typical deuterium enrichment described by Sofer (1978) and Bath et al. (1987) for gypsum formed diagenetically by hydration of anhydrite (Fig. 2f).

Figure 3 presents the $\delta^{34}\text{S}$ and $\delta^{18}\text{O}$ of the dissolved sulfate ion in equilibrium with 127 gypsum samples from the investigated Primary Lower Gypsum and Upper Gypsum units, considering the sulfur (Thode and Monster, 1965; Raab and Spiro, 1991) and oxygen (Lloyd, 1968; Van Driessche et al., 2016) isotope fractionations between the dissolved sulfate ion and gypsum ($\varepsilon^{34}\text{S}_{\text{SO}_4-\text{GYP}} = -1.65 \text{ ‰}$ and $\varepsilon^{18}\text{O}_{\text{SO}_4-\text{GYP}} = -3.6 \text{ ‰}$, respectively). Most of the $\delta^{34}\text{S}$ values of dissolved SO_4^{2-} deduced from Primary Lower Gypsum and Upper Gypsum deposits span a range of 2‰, centered around 22‰ vs CDT, which corresponds to the $\delta^{34}\text{S}$ of the SO_4^{2-} ion dissolved in the Messinian ocean (Masterson et al., 2016). The $\delta^{18}\text{O}$ compositions of dissolved SO_4^{2-} deduced from Primary Lower Gypsum and Upper Gypsum deposits span a larger range of about 8‰ (excluding one very ^{18}O -depleted Primary Lower Gypsum sample from the Arnulfi section), from 6 to 15 ‰ vs SMOW, which includes the $\delta^{18}\text{O}$ of the SO_4^{2-} ion dissolved in the Messinian Ocean (Turchyn and Schrag, 2004). The dissolved sulfate ion corresponding to Messinian gypsum is isotopically heavier than that corresponding to older gypsum deposits (> 14 million years old) formed from evaporation of ocean water that was considerably more ^{34}S - and ^{18}O -depleted compared to the Messinian ocean (Utrilla et al., 1992) (Fig. 3). Compared to the range of $\delta^{34}\text{S}_{\text{SO}_4}$ and $\delta^{18}\text{O}$ values in modern sediment pore waters where microbial sulfate reduction is active (blue area in figure 3) (Fotherby et al., 2021), the range of $\delta^{34}\text{S}_{\text{SO}_4}$ corresponding to Primary Lower Gypsum and Upper Gypsum deposits is limited (Fig. 3).

5. Modelling: approaches and results

5.1 Modelling the evaporation of seawater

We first tested the ability of the model to reproduce the isotope composition of gypsum ($\delta^{18}\text{O}_{\text{H}_2\text{O}}$ and $\delta\text{D}_{\text{H}_2\text{O}}$) formed in modern Mediterranean salt works (Fontes, 1966; Fontes and Gonfiantini, 1967; Longinelli, 1979; Evans et al., 2015) (Fig. 2). In this base-case evaporation scenario, the atmospheric conditions that control isotope effects during evaporation (Supplementary Table 11) are based on an isotopic study of atmospheric water vapor in the Vaccarès Lagoon (Camargue Area, southern France) (Delattre et al., 2015), located 25 km away from the Aigues-Mortes salt works (Fontes, 1966; Fontes and Gonfiantini, 1967) (Fig. 1). These conditions include an elevated water temperature (29°C), a low atmospheric relative humidity (0.46) and a low wind speed (1.43 m s⁻¹). Neglecting mixing with continental

runoff, modern Atlantic Ocean water in front of Gibraltar ($\delta^{18}\text{O} = 1\text{ ‰}$ vs SMOW; $\delta\text{D} = 6\text{ ‰}$ vs SMOW, salinity = 36.4 g/kg; Benetti et al. 2017a) was allowed to evaporate. The path in the $\delta^{18}\text{O}$ - δD space is shown as green lines in the panels of Fig. 2, while the gypsum saturation point is marked as a green dot within a black circle at the end of the evaporation path. For this base-case scenario, the gypsum saturation point is attained when salinity is equal to 115 g kg^{-1} (data not shown), $\delta^{18}\text{O}_{\text{H}_2\text{O}}$ is equal to 7.71 ‰ vs SMOW and $\delta\text{D}_{\text{H}_2\text{O}}$ is equal to 32.32 ‰ vs SMOW (Fig. 2). This water isotope composition falls within the range of values observed in modern Mediterranean salt works, showing that the model correctly simulates this relatively constrained evaporative system.

The two key parameter settings that result in a good fit of the numerical model to the salt work gypsum parent water isotopes are a low atmospheric relative humidity (46%) and a low wind speed (1.4 m/s). Both these parameter settings produce a strong deuterium excess in the evaporative flux and thus a strong deuterium depletion of the residual water body (see Supplementary Material). The evolution of salinity and water isotopes after the point of gypsum saturation, when water isotopes are affected considerably by the fractionation between free water molecules and water molecules in the hydration sphere of dissolved ions (Sofer and Gat, 1972, 1975), is represented by a green dotted line. Note that the influence of the salt effect becomes important only after the gypsum saturation point is attained.

The model was then forced considering the physical and chemical boundary conditions representative of the modern open Mediterranean Sea that are different from the more continental ones of the Vaccarès Lagoon (Supplementary Figure 2). These boundary conditions are taken from the geographically-resolved (0.25 degree intervals for both latitude and longitude), monthly averages of climate variables (sea-surface temperature, air temperature, wind speed, atmospheric pressure and atmospheric humidity) provided by the ERA5 reanalysis of the European Centre for Medium-Range Weather Forecast (ECMWF), and from Mediterranean Sea (Gat et al., 2003) and north Atlantic (Benetti et al., 2017b) atmospheric water vapor isotope measurements, as explained in the Supplementary Material. Altogether, we carried out three sets of 1517 model runs each, representative of the geographically-resolved, 30-year (1990-2019) average climatology for the months of January and of July, and of the average yearly climatology for the same 30-year period. In figure 2f the water isotope composition calculated by the evaporation model at gypsum saturation for these three groups of boundary conditions are shown as blue (average July), green (average

January) and red (average yearly) dots. In all of the considered model runs, the evaporation model calculates a salinity of $\sim 115 \text{ g kg}^{-1}$ at the gypsum saturation point (data not shown).

Evaporation of Atlantic Ocean waters under the considered Mediterranean Sea conditions results in a range of water isotope compositions at gypsum saturation, ranging from values approaching those of the initial fluid ($\delta^{18}\text{O} = 1\text{ ‰}$ vs SMOW; $\delta\text{D} = 6\text{ ‰}$ vs SMOW) in summer conditions (Fig. 2f, blue dots), to values ($> 7\text{ ‰}$ vs SMOW) heavier than gypsum parent waters formed in salt works in winter conditions (Fig. 2f, green dots). Under July and average yearly conditions, the model water isotope composition at gypsum saturation (Fig. 2f, red dots) has a $\delta^{18}\text{O}$ comparable to that of the gypsum parent waters of the Santa Elisabetta and Eraclea Minoa sections of the Caltanissetta basin, the Monte Tondo quarry section of the Vena del Gesso, the Volterra basin and the Banengo section of the Piedmont basin (Fig. 2; Table 1), although it is up to 20 ‰ enriched in deuterium compared to gypsum parent waters of these Messinian sections. The calculated water isotope composition under average yearly conditions, however, are considerably heavier than the isotope compositions of gypsum parent waters from the Arnulfi and Pollenzo sections of the Piedmont basin (Fig. 2; Table 1). These results put limits to the use of gypsum parent water isotope compositions as indicators of gypsum parent water salinity (see discussion in section 6.2).

5.2 Modelling the evaporation of mixtures of seawater and continental runoff

Since there is ample geochemical evidence that continental runoff contributed significant volumes of water to the Mediterranean Sea during the deposition of the Primary Lower Gypsum and Upper Gypsum units (Flecker et al., 2002; Topper et al., 2011, 2014; Roveri et al., 2014; Reghizzi et al., 2018), we tested the effect on model output of the mixing of ion-free meteoric waters with Atlantic waters prior to evaporation. All the model runs in this section were carried out at a temperature of 20°C (representative of average Mediterranean surface water temperature; Supplementary Figure S2), to single out the effect of mixing with continental runoff on model results. We *a priori* considered the average rain water isotope composition of the Almeria region (IAEA, 2005; Evans et al., 2015), where the Sorbas basin is located, mixed it in four different proportions ($f_R = 0.2, 0.4, 0.6$ and 0.9) with Atlantic waters, and calculated the salinity- $\delta^{18}\text{O}_{\text{H}_2\text{O}}$ evolution to the point of gypsum saturation (red lines in figure 4). The physical conditions forcing evaporation were calculated as the average of all 1517 points used in the 30-year yearly average climatology (Supplementary Table 11). The addition of ion-free meteoric waters results in an initial fluid with a higher degree of under-saturation with respect to gypsum, and thus necessitating a larger degree of evaporation

to reach saturation, but also to lower initial salinity and isotopically lighter water isotope composition. Thus, such addition of ion-free meteoric waters to the initial fluid changes neither the salinity ($\sim 115 \text{ g kg}^{-1}$) or the water isotope composition ($\delta^{18}\text{O} \sim 4 \text{ ‰}$ vs SMOW) of the gypsum saturation point (Fig. 4).

In these conditions, the mixing-evaporation model calculates a strong under-saturation with respect to gypsum ($0.06 < \Omega_{\text{Gypsum}} < 0.32$) at the salinity corresponding to that of the fluid inclusions of low-salinity Primary Lower Gypsum and Upper Gypsum deposits (red lines in Fig. 4b). We carried out additional model runs to test if the presence of dissolved Ca^{2+} and SO_4^{2-} in continental runoff depressed the salinity at the point of gypsum saturation (dotted blue lines in figure 4). First, we repeated the above-mentioned model runs adding 5 mM dissolved Ca^{2+} and SO_4^{2-} in the continental runoff end member. This set of model runs shows that the presence of dissolved Ca^{2+} and/or SO_4^{2-} in the freshwater endmember depresses the salinity at gypsum saturation (Fig 4b): as the runoff/ocean water ratio f_R increases from 0.4 to 0.9, this effect increases in magnitude.

We considered two main sources of poorly-saline, Ca^{2+} - and SO_4^{2-} -bearing fluids pertinent to our Mediterranean case (Table 2): (i) riverine input from Mediterranean Sea (principally Nile and Rhone) and Black and Caspian Seas rivers, based on recent studies suggesting that the Paratethys was a source of water for the Mediterranean Sea during the Messinian Salinity Crisis (Grothe et al., 2014, 2020; Marzocchi et al., 2016; van Baak et al., 2017), and supposing that the Paratethys was a freshwater lake; (ii) modern Caspian Sea water, based on the idea (Grothe et al., 2020) that the Paratethys flowing into the Mediterranean during the Messinian Salinity Crisis had a chemical composition similar to that of the modern Caspian Sea (salinity $\sim 12 \text{ g kg}^{-1}$ and dissolved Ca^{2+} and SO_4^{2-} similar to modern seawater). In this set of model runs, to track the runoff/ocean water mixing ratio with geochemically measurable quantities, we consider the isotope tracers $^{87}\text{Sr}/^{86}\text{Sr}$ and $\delta^{34}\text{S}_{\text{SO}_4}$. The use of Sr isotopes to track mixing of Atlantic Ocean water with continental runoff is straightforward because Sr is not involved in biogeochemical processes and Sr isotopes do not fractionate during gypsum precipitation (Flecker et al., 2002; Topper et al., 2011; Grothe et al., 2020). The $^{87}\text{Sr}/^{86}\text{Sr}$ composition of the continental runoff end members is summarized in table 2. The $^{87}\text{Sr}/^{86}\text{Sr}$ composition calculated by the model is compared to the $^{87}\text{Sr}/^{86}\text{Sr}$ of gypsum from the Primary Lower Gypsum and Upper Gypsum units presented in Roveri et al. (2014).

In addition to mixing between the oceanic and continental SO_4^{2-} sources, the $\delta^{34}\text{S}_{\text{SO}_4}$ of dissolved SO_4^{2-} , however, is affected by biogeochemical processes of the S cycle (sulfate

reduction, sulfide oxidation, disproportionation...) taking place in sediments or water column during the Messinian Salinity Crisis (Pierre, 1982; Lu, 2006; Garcia-Veigas et al., 2018).

Although a large S-isotope fractionation ($5 < \varepsilon_{\text{SR}} \text{‰} < 70$; Sim et al., 2011; Leavitt et al., 2013) is associated to SO_4^{2-} -consumption via sulfate reduction, resulting in a ^{34}S -enrichment of the residual SO_4^{2-} pool, successive biogeochemical-production of SO_4^{2-} via re-oxidation of H_2S can at most, in the case of a geochemically closed system, bring the $\delta^{34}\text{S}_{\text{SO}_4}$ of the dissolved SO_4^{2-} pool back to its original, unreacted value (Aller et al., 2010; Mills et al., 2016; Blonder et al., 2017). Therefore, the biogeochemical sulfur cycle rarely results in a net decrease of $\delta^{34}\text{S}$ of dissolved SO_4^{2-} and the $\delta^{34}\text{S}_{\text{SO}_4}$ of Primary Lower Gypsum and Upper Gypsum deposits can be used to track the ^{34}S -depleted continental SO_4^{2-} source introduced into the Mediterranean basin by continental runoff or via the Paratethys. To this end we compiled available published $\delta^{34}\text{S}_{\text{SO}_4}$ data from Primary Lower Gypsum and Upper Gypsum deposits and, together with the data presented in this work (Fig. 5), we defined a lower boundary for the $\delta^{34}\text{S}_{\text{SO}_4}$ of Primary Lower Gypsum and Upper Gypsum that we use as a constraint to the mixing proportions between oceanic and continental SO_4^{2-} imposed in the model calculations.

Figure 6 shows how the salinity at gypsum saturation, the $^{87}\text{Sr}/^{86}\text{Sr}$ and the $\delta^{34}\text{S}_{\text{SO}_4}$ of Mediterranean Sea waters are affected by the runoff/ocean water mixing ratio, the concentration of riverine dissolved Ca^{2+} , SO_4^{2-} and Sr^{2+} , and the isotope composition of riverine dissolved Sr ($^{87}\text{Sr}/^{86}\text{Sr}$). The isotope composition of riverine dissolved SO_4^{2-} ($\delta^{34}\text{S}_{\text{SO}_4}$) was set equal to 8 ‰ vs CDT, corresponding to the average $\delta^{34}\text{S}_{\text{SO}_4}$ of the Volga and Danube rivers (Mekhtieva and Rabinovich, 1975) ($\delta^{34}\text{S}_{\text{SO}_4}$ for Mediterranean large rivers is not documented). The evaporation model complemented by these isotope systems was run 3000 times with different combinations of the forcing parameters listed above. Solutions to the model runs are presented in six diagrams corresponding to runoff/ocean water mixing ratios equal to 0.9 (Fig. 6a and 6b), 0.6 (Fig. 6c and 6d) and 0.4 (Fig. 6e and 6f). Isolines of salinity at gypsum saturation are represented as red lines in figures 6a, 6c and 6e and are read as a function of the riverine dissolved SO_4^{2-} (y axis) and Ca^{2+} (x axis) concentration. In the same diagrams the $\delta^{34}\text{S}_{\text{SO}_4}$ of dissolved sulfate in the mixture is represented by horizontal dashed blue lines; the blue shaded area represents the range of salinities measured from fluid inclusions in gypsum from the Primary Lower Gypsum and Upper Gypsum units (Natalicchio et al., 2014; Evans et al., 2015; Costanzo et al., 2019); the red dashed box represents the dissolved Ca^{2+} and SO_4^{2-} concentration in main rivers entering the Mediterranean, Black and

Caspian seas (Table 2); the vertical orange and green bars represent the $\delta^{34}\text{S}$ of dissolved SO_4^{2-} deduced from isotope measurements of gypsum from the Primary Lower Gypsum and Upper Gypsum units (Fig. 5), while the red dot corresponds to the dissolved Ca^{2+} and SO_4^{2-} in the modern Caspian Sea. In Fig 6b, 6d and 6f, the blue contours represent the calculated $^{87}\text{Sr}/^{86}\text{Sr}$ of dissolved Sr^{2+} as a function of the riverine dissolved Sr^{2+} concentration (x-axis) and isotope composition ($^{87}\text{Sr}/^{86}\text{Sr}$) (y-axis); the orange and light blue shaded areas represent the $^{87}\text{Sr}/^{86}\text{Sr}$ range of Primary Lower Gypsum and Upper Gypsum deposits, respectively (Roveri et al., 2014); the red dots represent the Sr flux-weighted dissolved Sr concentration and $^{87}\text{Sr}/^{86}\text{Sr}$ of runoff considering only the Nile and the Rhone rivers (Nile/Rhone), only rivers draining into the modern Black ad Caspian seas (BS/CS rivers), and all of these sources (All rivers) (Table 2).

Dissolved Ca^{2+} and SO_4^{2-} concentrations in the range of modern Mediterranean and Caspian/Black Sea rivers (red dashed box in Fig. 6a, 6c and 6e), coupled to a very high runoff fraction ($f_R = 0.9$), result in a salinity at gypsum saturation that overlaps with the highest salinities ($45 < \text{S g kg}^{-1} < 78.2$) deduced for Primary Lower Gypsum and Upper Gypsum deposits based on gypsum fluid inclusions (Costanzo et al., 2019; Evans et al., 2015; Natalicchio et al., 2014; this work) (blue area in Fig. 6a, 6c and 6e). With these Ca^{2+} and SO_4^{2-} concentrations, the salinity at saturation remains higher than the average salinity of Primary Lower Gypsum and Upper Gypsum fluid inclusions from the Piedmont basin (16 g kg^{-1}) (Natalicchio et al., 2014), the Catanzaro Trough (27 g kg^{-1}) (Costanzo et al., 2019) and the Sorbas Basin (32 g kg^{-1}) (Evans et al., 2015). Only the average salinity of the Vena del Gesso fluid inclusions (52.2 g kg^{-1} ; this work) is compatible with $f_R = 0.9$ and the dissolved Ca^{2+} and SO_4^{2-} concentration of modern Mediterranean and Caspian/Black Sea rivers. With these riverine fresh water sources, however, the final mixture has $^{87}\text{Sr}/^{86}\text{Sr}$ comparable to that of Upper Gypsum deposits (Fig. 6b), which are more ^{87}Sr -depleted than the Vena del Gesso Primary Lower Gypsum deposits. On the other hand, imposing f_R values lower than 0.9 (Fig. 6c and 6e), dissolved Ca^{2+} and SO_4^{2-} concentrations in the range of modern Mediterranean and Caspian/Black Sea rivers result in salinities higher than those of Primary Lower Gypsum and Upper Gypsum fluid inclusions. On this basis, we can exclude that the small amounts of riverine dissolved Ca^{2+} and SO_4^{2-} derived from weathering of carbonates and pyrite can be the trigger for the precipitation of low-salinity gypsum in Mediterranean marginal basins.

With a runoff component having the dissolved Ca^{2+} and SO_4^{2-} composition of the modern Caspian Sea (red dot in Fig. 6a, 6c and 6e), the salinity at gypsum saturation is considerably

depressed at all three f_R values ($14 < S \text{ g kg}^{-1} < 66$) and covers most of the range of salinities found in Primary Lower Gypsum and Upper Gypsum fluid inclusions (Natalicchio et al., 2014; Evans et al., 2015; Costanzo et al., 2019). However, since the modern Caspian Sea has an elevated dissolved SO_4^{2-} concentration (30 mM; Table 2), the resulting $\delta^{34}\text{S}_{\text{SO}_4}$ of the seawater-runoff mixture is low and varies from 9 ‰ vs CDT ($f_R = 0.9$) to 16 ‰ vs CDT ($f_R = 0.4$). Therefore, for all considered values of f_R , the $\delta^{34}\text{S}_{\text{SO}_4}$ of the resulting seawater-runoff mixture is considerably lower than that deduced from $\delta^{34}\text{S}_{\text{SO}_4}$ measurements of both Primary Lower Gypsum and Upper Gypsum deposits ($20.15 < \delta^{34}\text{S}_{\text{SO}_4} \text{ vs CDT } < 23.7$) (Fig. 6a, 6c and 6e). As discussed in section 6.4, these results provide a quantitative basis for evaluating the influence of the Paratethys in the formation of low-salinity gypsum (Grothe et al., 2020).

6. Interpretation and Discussion

6.1 Primary versus diagenetic origin of the “low-salinity” geochemical signal

Based on the absence of macro- and microscale evidence for recrystallization of gypsum (e.g. Fig. 7), we can exclude that pervasive dissolution-reprecipitation processes or dehydration/rehydration cycles have reset the gypsum crystallization water isotope composition (see supplementary material for a full discussion of gypsum diagenesis). Indeed, a simple isotope mass balance calculation (Table 3) implies that if the measured isotope composition of gypsum samples was the result of diagenetic alteration of an original, evaporitic gypsum (with crystallization water $\delta^{18}\text{O} \sim 6.5 \text{ ‰}$ vs SMOW) under the influence of meteoric fluids ($-9 < \delta^{18}\text{O} \text{ ‰}$ vs SMOW < -5.11 ; Table 3), then from 5% to 87% of the gypsum in the analyzed samples would have suffered intense post-depositional alteration. Petrographic analyses of the crystals carried out on 15 polished slabs and 30 thin slices (see supplementary methods), however, do not show any evidence for a pervasive recrystallization process, but rather suggest the perfect preservation of delicate pristine features of the crystals such as filamentous microfossils and diatom remains (e.g., Pellegrino et al., 2021).

As for the fluid inclusion salinity signal, it can potentially be reset by leaking of the fluid inclusions and partial refilling with meteoric waters, without affecting the isotope composition of gypsum crystallization water. However, we are confident that the studied samples are mostly not affected by such a contamination for the following reasons: (1) we have measured fluid inclusions of different sizes (10 to 60 μm wide, with an area approximately ranging from 100 to 3500 μm^2), without optical evidence of modification (i.e. irregular shape of the inclusions, fractures); (2) we systematically excluded fluid inclusions

located near fluid inclusion families of clear secondary origin (see supplementary methods for petrographic criteria used to discriminate primary from secondary fluid inclusions); (3) we have carried out an exploratory cathodoluminescence survey of what we interpret as primary and secondary fluid inclusions based on petrographic evidence. We observed no difference of luminescence between the primary fluid inclusions and the surrounding gypsum. In contrast, different generations of secondary fluid inclusions (both trails along fractures and fluid inclusion families placed along the main gypsum cleavage plains) show occasionally a pale to bright orange luminescence (supplementary figure S3) suggesting the presence of carbonate phases precipitated from post-depositional groundwater fluids. Overall, these observations confirm that the studied primary fluid inclusions still retain their primary chemical composition.

These results have to be weighed in the light of a recent work by Bigi et al. (2022) that applies a new microthermometric protocol for fluid inclusion analysis of Messinian gypsum samples, arguing against the low-salinity scenario for marginal basin Messinian gypsum deposits. Bigi et al. (2022) propose that the more reliable salinity data, falling in the classical gypsum precipitation salinity field (salinity $> 110 \text{ g kg}^{-1}$), are from the smallest fluid inclusions (with area $< 700 \mu\text{m}^2$), while larger fluid inclusions, that include those bearing the low-salinity signal, are more likely affected by leaking and refilling processes. However, both in Natalicchio et al. (2014), as well as in the present study, we have measured numerous primary fluid inclusions falling in the $< 700 \mu\text{m}^2$ size class that have salinities well below a typical evaporated, gypsum-saturated seawater. Further, the new microthermometric protocol proposed by Bigi et al (2022) implies a strong thermal stretching consisting in several cooling-heating cycles (thermal shock, from -100 to + 120°C) with the aim to nucleate a small vapor bubble within the inclusions that reduce their metastable behavior during microthermometric measurements. Such an approach largely differs from the weak stretching methodology used in this work which consisted in a single cooling-heating cycle (-90 to + 30°C), as suggested by previous studies (Attia et al., 1995; Natalicchio et al., 2014), in order to promote the nucleation of small bubbles while minimizing the loss of fluid from the inclusion. Indeed, especially after stretching, the fluid can be lost by diffusion from the inclusion, even in cases of low strain rate (e.g. Bodnar, 1993). We suspect that a strong thermal shock applied to soft gypsum crystals may cause an excessive stretching (i.e. increase in volume) with an irreversible re-equilibration of fluid inclusions. Experimental studies from aqueous fluid inclusions in quartz (Hall and Stern, 1993) showed that the water loss by

diffusion and mechanical micro-stretching resulted in an increase of the fluid inclusion salinity, despite the elevated hardness of this mineral. We therefore conclude that the fluid inclusion salinity and the isotopic composition of gypsum hydration water of Primary Lower Gypsum and Upper Gypsum deposits presented in this work represent a primary geochemical signal.

6.2 Updating existing evidence for low-salinity gypsum deposits during the Messinian Salinity Crisis

The new fluid inclusion data from the Vena del Gesso expands the existing evidence for gypsum from the Primary Lower Gypsum and Upper Gypsum units precipitated from low-salinity water masses (Natalicchio et al., 2014; Evans et al., 2015; Costanzo et al., 2019). Of the samples for which we do not have fluid inclusion data (Eraclea Minoa, Santa Elisabetta, Gibliscemi, Arnulfi and Pollenzo sections), some indications of formation from low-salinity parent waters come from the hydration water isotope composition. An intuitive - but wrong – interpretation, is that Messinian gypsum parent water isotope compositions significantly lighter than those of modern salt work gypsum (Fontes, 1966; Fontes and Gonfiantini, 1967; Longinelli, 1979; Evans et al., 2015) imply that Messinian gypsum was formed from low-salinity ($< 115 \text{ g kg}^{-1}$) water masses. Indeed, all gypsum parent waters from the considered marginal basins are isotopically lighter than those of gypsum formed by evaporation of seawater in modern Mediterranean Sea salt works (Fig. 2).

Our evaporation calculations, however, show that there is a strong continental influence on the hydration water isotope composition of gypsum formed in modern Mediterranean salt works (Fig. 2f). Both the Vaccarès Lagoon and the Aigues Mortes salt works are located 4 – 10 km inland from the coast, and experience more continental atmospheric conditions than those of the open Mediterranean Sea. Typically, atmospheric relative humidity and wind speed are lower over land than over the open ocean (Archer, 2005). Also, the water temperature imposed in the model to represent that of the Aigues Mortes salt work summer waters (29°C) is several degrees higher than the Mediterranean Sea summer surface temperature (22-27°C; Pastor et al., 2017).

Consistently, when average yearly or July evaporation conditions over the open Mediterranean Sea - that are more humid and windier than those at the Vaccarès Lagoon – are considered, the calculated isotope composition of water at the gypsum saturation point is up to several per mill lighter in ^{18}O and D than that of modern salt works (Fig. 2f). Thus, the parent water isotope composition of most of the samples from the Santa Elisabetta and

Eraclea Minoa sections fall in the same range of $\delta^{18}\text{O}_{\text{H}_2\text{O}}$ values calculated at gypsum saturation by the model forced by average yearly Mediterranean Sea conditions. For this reason, the gypsum samples from these two sections are compatible with formation from the evaporation of seawater to a salinity of 115 g kg^{-1} and cannot, based on our data, be interpreted as low-salinity gypsum. On the other hand, gypsum samples from the Pollenzo and Arnulfi sections of the Piedmont Basin, and the most ^{18}O -depleted samples from the Gibliscemi and the Santa Elisabetta sections in the Caltanissetta basin, have parent waters more ^{18}O -depleted than those calculated by the model at the gypsum saturation point. These gypsum samples have been formed from water masses: (i) that contained an important admixture of ^{18}O -depleted continental runoff, and (ii) that underwent only a limited extent of evaporation. These conditions imply that these are low-salinity gypsum deposits.

Altogether, four Mediterranean marginal basins - the Piedmont basin (Natalicchio et al., 2014), the Sorbas basin (Evans et al., 2015), the Catanzaro Trough (Costanzo et al., 2019) and the Vena del Gesso basin (this work) – contain gypsum deposits that, based on fluid inclusion salinity estimates, were formed from water masses that were far less saline than the salinity at which gypsum starts to precipitate from evaporating seawater ($\sim 110 \text{ g kg}^{-1}$) (Table 2). In addition, gypsum from the Pollenzo and Arnulfi section of the Piedmont basin, and the most ^{18}O -depleted samples from the Gibliscemi and Santa Elisabetta sections, can be interpreted as low-salinity gypsum deposits based on the isotope composition of gypsum hydration water. The overwhelming majority of evidence for the occurrence of low-salinity gypsum comes from Primary Lower Gypsum, rather than Upper Gypsum deposits.

6.3 Recycling of older gypsum deposits

The apparent contradiction of gypsum deposits bearing geochemical signatures that indicate precipitation from a poorly saline water mass has been explained by the leaching of older, exposed gypsum deposits and the precipitation of the released SO_4^{2-} and Ca^{2+} ions in adjacent basins (Attia et al., 1995; Ayora et al., 1995; Cendón et al., 2004). The recycling process can be easily tracked when the pre-existing gypsum is much older and bears a $\delta^{34}\text{S}_{\text{SO}_4}$ signature that is distinct (usually ^{34}S -depleted; see figure 3) compared to the neo-formed gypsum deposit. This is the case of gypsum from the Upper Eocene South Pyrenean Basin (Ayora et al., 1995), formed by recycling of Upper Triassic ^{34}S -depleted gypsum deposits. This recycling process led to the deposition of gypsum with a very low $\delta^{34}\text{S}_{\text{SO}_4}$ ($12.95 < \delta^{34}\text{S}_{\text{SO}_4} \%$ vs CDT < 19.27) compared to primary gypsum formed in the same basin by precipitation from seawater (average $\delta^{34}\text{S}_{\text{SO}_4} = 21.6$). Recycling of Upper Triassic evaporites was also

reported for the deposition of the upper Miocene gypsum of intramontane Neogene Betic basins, such as the Lorca and Fortuna basins (Playa et al., 2000; Garcia-Veigas et al., 2020). For the Primary Lower Gypsum and Upper Gypsum deposits studied here, recycling of older gypsum can be, however, ruled out, based on the late Miocene $\delta^{34}\text{S}_{\text{SO}_4}$ signature of these deposits.

The effect of recycling on the $\delta^{34}\text{S}_{\text{SO}_4}$ of gypsum is undetectable when the recycling takes place intra-basinally and thus the original, weathered primary gypsum has the same age, and the same $\delta^{34}\text{S}_{\text{SO}_4}$, as the neo- precipitated gypsum. This is the case described by Attia et al. (1995) to explain primary gypsum deposits from the Middle Miocene of Egypt (Gulf of Suez) with $\delta^{34}\text{S}_{\text{SO}_4}$ (21.9 to 23.6 ‰ vs CDT) indicating a marine SO_4^{2-} source but low-salinity fluid inclusions. A similar scenario was proposed for the low salinity Badenian (Cendón et al., 2004) and Messinian primary marine gypsum (Evans et al., 2015), including the Piedmont gypsum studied here (Banengo section, Natalicchio et al., 2014). However, no geological evidence of coeval marine evaporitic gypsum that was leached to provide the ions necessary for the precipitation of the observed low salinity gypsum has been reported, making this explanation unlikely and not supported by field data. Moreover, the majority of the oldest evaporitic deposits that we analyzed, i.e those from the 1st Primary Lower Gypsum cycle from the Monticino (Vena del Gesso) and Banengo and Arnulfi (Piedmont Basin) sections have fluid inclusion salinity or hydration water isotopes that indicate formation from low-salinity water masses (most of the gypsum hydration water isotopes from the S. Elisabetta section are inconclusive as to the salinity of the parent waters, see above): the hypothetical, original marine gypsum deposits that would have been leached are missing.

6.4 Ca- and SO_4 -rich Paratethys inflow during the Messinian Salinity Crisis

Based on $^{87}\text{Sr}/^{86}\text{Sr}$ isotope evidence for a connection between the Paratethys and the Mediterranean Sea starting from 6.1 Ma, Grothe et al. (2020) propose that brackish water flowing into the Mediterranean Sea from the Paratethys formed a surface layer that underwent little or no mixing with the underlying Mediterranean high-salinity water. The brackish surface layer filled Mediterranean marginal basins where it formed low-salinity gypsum by evaporation. The key to this scenario is that modern Caspian Sea water, taken to represent Paratethys water during the Messinian Salinity Crisis (Grothe et al., 2020), has a salinity ranging from 10 to 15 g kg⁻¹, but dissolved Ca^{2+} and SO_4^{2-} concentrations similar to modern seawater ($\sim 8 \text{ mol kg}^{-1}$ and $\sim 30 \text{ mol kg}^{-1}$, respectively). By evaporating this water, and a

modified version without dissolved Na^+ and Cl^- , gypsum saturation is attained at 45 g kg^{-1} and 14 g kg^{-1} , respectively (Grothe et al., 2020).

Several lines of evidence, however, suggest that the existence of such a Ca^{2+} - and SO_4^{2-} -rich Paratethyan source is unlikely. First, if Paratethys waters flowing into the Mediterranean Sea and into its marginal basins did not mix with the underlying Mediterranean water mass, as the evaporation calculations of Grothe et al. (2020) suppose, then they should have retained the $^{87}\text{Sr}/^{86}\text{Sr}$ signature of the Paratethys ($\sim 0.7084 - 0.7085$; Grothe et al. 2020). This is not the case because gypsum from the Primary Lower Gypsum unit shows a uniform $^{87}\text{Sr}/^{86}\text{Sr}$ signature that is more radiogenic ($0.708640 < ^{87}\text{Sr}/^{86}\text{Sr} < 0.709024$) than the Paratethys Sr source, implying mixing with Atlantic-derived Sr ($^{87}\text{Sr}/^{86}\text{Sr} \sim 0.7090$; McArthur et al., 2001). In addition to changing the $^{87}\text{Sr}/^{86}\text{Sr}$, mixing of the Paratethys source with Atlantic Ocean waters would have increased the salinity of the mixture. Second, as our model calculations show (section 5.2), lack of mixing between the Paratethys input and Atlantic waters would result in a strongly ^{34}S -depleted dissolved sulfate ion similar to the one of the rivers flowing into the Black and Caspian Seas ($0.7 < \delta^{34}\text{S}_{\text{SO}_4} \text{‰ vs CDT} < 7.6$; Table 3), or the modern Caspian Sea ($\delta^{34}\text{S}_{\text{SO}_4} = 8.7 \text{‰ vs CDT}$). However, this is not the case because all Primary Lower Gypsum and Upper Gypsum deposits have $\delta^{34}\text{S}_{\text{SO}_4}$ values indicating a marine SO_4^{2-} source ($20.4 < \delta^{34}\text{S}_{\text{SO}_4} \text{‰ vs CDT} < 23.7$; Fig. 3).

In our modeling exercise discussed in section 5.2, the least well-constrained forcing parameter is the dissolved Ca^{2+} concentration of the non-oceanic source. The modern rivers flowing into the Mediterranean, Black and Caspian Seas all have dissolved Ca^{2+} concentrations $\leq 2 \text{ mM}$ (Table 3). With these dissolved Ca^{2+} concentrations, and the constraints imposed by the $^{87}\text{Sr}/^{86}\text{Sr}$ and $\delta^{34}\text{S}_{\text{SO}_4}$ signature of gypsum deposits, the model always calculates a salinity at gypsum saturation greater than 60 g kg^{-1} (Fig. 6). Since it is likely that dissolved Ca^{2+} concentrations in Messinian rivers feeding the Mediterranean, Black and Caspian Seas during the Messinian Salinity Crisis were not radically different from the modern values, we can exclude that Ca^{2+} - and SO_4^{2-} -bearing continental runoff is responsible for the formation of low-salinity gypsum. The only alternative, potentially Ca-rich, brackish water source is the Paratethys. Accepting Sr-isotope evidence suggesting a hydrological connection between the Mediterranean Sea and the Paratethyan Black Sea and Caspian domains during the Messinian Salinity Crisis (Grothe et al., 2020), the idea that the modern chemical composition of the Caspian Sea - brackish, but Ca^{2+} - and SO_4^{2-} -rich - is representative of the Paratethys during the Messinian Salinity Crisis needs to be evaluated.

The Caspian Sea has been an endoreic basin during the past ~ 3 Myr (Palcu et al., 2019). Its modern chemical composition has thus been acquired during 3 Myr of ion addition by rivers and ion extraction by chemical and biogeochemical processes (Berner and Berner, 2012): its high Ca^{2+} and SO_4^{2-} concentrations are the consequence of isolation. Prior to the connection of the Paratethys to the Mediterranean (before 6.1 Ma) a few $^{87}\text{Sr}/^{86}\text{Sr}$ data points from the Black and Caspian Sea domains indicate that $^{87}\text{Sr}/^{86}\text{Sr}$ in the Paratethys was low (~ 0.708025) relative to coeval oceanic and Mediterranean Sea $^{87}\text{Sr}/^{86}\text{Sr}$ (~ 0.709). This low Paratethyan $^{87}\text{Sr}/^{86}\text{Sr}$ signature is very similar to the Sr flux-weighted $^{87}\text{Sr}/^{86}\text{Sr}$ of modern Sr riverine input into the Black and Caspian seas ($[\text{Sr}^{2+}] = 4.92 * 10^{-6}$ mol/litre ; $^{87}\text{Sr}/^{86}\text{Sr} = 0.708215$). This supports the idea that also prior to 6.1 Ma the Paratethys was a large endoreic water mass that potentially had high dissolved Ca^{2+} and SO_4^{2-} concentration similar to that of the modern Caspian Sea.

At roughly 6.1 Ma, $^{87}\text{Sr}/^{86}\text{Sr}$ in the Paratethyan domain rises sharply reaching values similar to coeval Mediterranean water, suggesting a connection with the Mediterranean (confirmed by eastern Mediterranean biomarker studies; Vasiliev et al. (2019), and then decrease to about 0.7084-0.7085 during the whole of the Messinian Salinity Crisis. These intermediate $^{87}\text{Sr}/^{86}\text{Sr}$ Messinian Salinity Crisis values are taken to represent mixing between the Paratethyan and Mediterranean Sea Sr (Grothe et al., 2020). Supposing that prior to the 6.1 Ma connection the chemical composition of the Paratethys was similar to that of the modern Caspian Sea (Clauer et al., 2000; Grothe et al., 2020), could this “endorheic” composition of the Paratethys have persisted throughout the 130 kyr preceding the Messinian Salinity Crisis onset when the Paratethys and the Mediterranean Sea were connected? The order-of-magnitude calculation that follows excludes this possibility.

The volume of the Paratethys at the end of the Miocene is estimated to have been between 0.5 and $1 \times 10^6 \text{ km}^3$ (de la Vara et al., 2016). With a late-Miocene Paratethys freshwater excess equal 0.02 Sv ($= 0.02 \times 10^6 \text{ m}^3/\text{s}$) (Marzocchi et al., 2016), the whole water volume of the Paratethys would have been replaced 80 to 160 times in 130 kyr that preceded the Messinian Salinity Crisis onset. The endorheic character of Caspian Sea chemistry, acquired prior to the connection with the Mediterranean, would therefore have been washed away before the onset of the Messinian Salinity Crisis. Should the Paratethys-Mediterranean connection have been a one-way flow of water directed to the Mediterranean, then the Paratethys would have been transformed into a lake having the chemical composition corresponding to the average composition of the riverine input. If, instead, as Sr-isotopes (Grothe et al., 2020) suggest, a

two-way water exchange flow with the Mediterranean Sea existed, then the Paratethys would have rapidly acquired normal marine $\text{Ca}^{2+}/\text{Cl}^-$ and $\text{SO}_4^{2-}/\text{Cl}^-$ ratios by the onset of the Messinian Salinity Crisis. These considerations exclude that the Paratethys source of freshwater carried a dissolved Ca^{2+} concentration higher than that of the rivers that fed the Paratethys (< 2 mM); they also explain why gypsum from the Primary Lower Gypsum and Upper Gypsum units lacks a continental, strongly ^{34}S -depleted isotope signature.

6.5 Does the biogeochemical sulfur cycle play a role in the formation of low-salinity gypsum?

In this section we will develop on the idea originally proposed by Dela Pierre et al. (2014, 2015), and successively by Grothe et al. (2020), that the biogeochemical sulfur cycle is involved in the formation of Mediterranean low-salinity gypsum deposits.

6.5.1 Biogeochemically active Messinian Salinity Crisis marginal basins

Evidence from a large number of studies using complementary approaches, especially from the Primary Lower Gypsum unit, suggests that low-salinity gypsum deposits accumulated in biogeochemically active marginal basins. Both bottom grown selenite crystals and the marly interbeds of the Primary Lower Gypsum unit deposits contain fossils of densely-packed filamentous organisms (“spaghetti-like” structures) (Vai and Ricci Lucchi, 2006; Panieri et al., 2010) (Fig. 7), that are also found in carbonate and shale layers considered as the lateral, deep-basin time-equivalents of gypsum layers of the Primary Lower Gypsum unit (Oliveri et al., 2010; Dela Pierre et al., 2012; Caruso et al., 2015; Natalicchio et al., 2017, 2019).

Recently the filaments were interpreted as being the fossil remains of giant colorless sulfide-oxidizing bacteria (CSB) like *Beggiatoa* and *Thioploca* on the basis of morphological features (size, hollowness, curved shape and internal segmentation) (Schopf et al., 2012; Dela Pierre et al., 2014, 2015) and the presence of iron sulfide and polysulfide inclusions within the filaments. Such inclusions were interpreted to represent the product of early diagenetic transformations of sulfur globules stored within the cells (Dela Pierre et al., 2015). The sulfur globules correspond to an intermediate product of the oxidation of sulfide to sulfate and are a clade diagnostic feature of colorless sulfide-oxidizing bacteria (Huettel et al., 1996; Schulz and Jorgensen, 2001; Teske and Nelson, 2006). The assignment of the filamentous fossils to this group of bacteria suggests that the basin floor where most of the Messinian gypsum grew was covered by a benthic assemblage of chemotrophic bacteria involved in an intense sulfur cycle. Besides, filamentous microfossil-bearing gypsum crystals contain abundant nano-sized planktic diatoms that reflects conditions of high primary productivity in the upper water

column. These diatoms represented a probable source of organic matter exploitable by benthic bacteria (Pellegrino et al., 2021). In addition, both gypsum and the interbedded marls contain organic-rich aggregates interpreted as marine snow floccules formed by aggregation of clay and organic material in the upper water column during episodes of eutrophication and phytoplankton blooms and deposited on an anoxic basin floor (Dela Pierre et al., 2014, 2015).

In the bottom grown selenite crystals of the Primary Lower Gypsum unit, filaments and floccules are entrapped in mm-thick turbid laminae that, in the re-entrant angle of the twinned crystals, alternate with limpid lamina typified by scarce or absent biogenic material (Fig. 7). Turbid laminae contain pyrite and dolomite grains (Dela Pierre et al., 2015) that are common by-products of microbial sulfate reduction. The lamination in the gypsum crystals is interpreted as the product of seasonal climate variability (Orti, 2011; Dela Pierre et al., 2015; Reghizzi et al., 2018). During the humid season, increased continental runoff favored water column stratification, high primary productivity and bottom oxygen depletion, favoring organic matter preservation in the sediments. Organic matter degradation by bacterial sulfate reduction provided the hydrogen sulfide flux required for the growth of CSB (Dela Pierre et al., 2015). The arid season was instead dominated by water column mixing and oxygenation of the water column (Dela Pierre et al., 2015). As discussed in the next section, such a seasonal alternation between oxidized and reduced conditions might have selected the benthic ecosystem in favor of metabolically flexible CSB communities.

Supplementary evidence for biogeochemical activity comes from the study of molecular fossils extracted from gypsum layers and marl interbeds of the Primary Lower Gypsum unit. The molecular fossil inventory of gypsum beds (hydrocarbons, alcohols, carboxylic acids) confirms that the mazes of filamentous microfossil are benthic microbial assemblages dominated by CSB associated to sulfate reducing bacteria (Natalicchio et al., 2022). The overall bacterial and archeal lipid inventory suggest the existence of a stratified marine basin (Natalicchio et al., 2022). With regards to the marl interbeds, molecular fossils include: (i) lipids produced by organisms that live at the interface between oxic and anoxic waters in stratified basins - including anoxygenic phototrophic bacteria - (Liaaen-Jensen, 1978; Kleemann et al., 1990; Sinninghe Damsté et al., 1995; Kenig et al., 1995; Rashby et al., 2007; Wakeham et al., 2007; Eickhoff et al., 2013), implying that anaerobiosis impinged on the photic zone during the deposition of marl interbeds (Tenhaven, 1989; Schoell et al., 1994; Sinninghe Damsté et al., 1995), and (ii) lipids with C and N isotope compositions implying that N_2 -

fixing diazotrophic cyanobacteria drove primary production during deposition of the marl interbeds (Isaji et al., 2019).

6.5.2 In search of a modern biogeochemical analogue

In modern marine environments, giant CSB like *Beggiatoa* and *Thioploca* thrive in organic-rich sediments such as in the Pacific Peru and the Atlantic Namibian continental margins (Jørgensen, 1977; Gallardo, 1977; Mussmann et al., 2003; Seitaj et al., 2015). These are areas of strong upwelling, where high primary productivity and water column stratification promote the formation of oxygen minimum zones (OMZs) in the water column (Schmaljohann et al., 2001; Callbeck et al., 2021). OMZs overlay organic-rich, sulfidic sediments characterized by high sulfate reduction rates (Gallardo et al., 1998; Schmaljohann et al., 2001; Callbeck et al., 2021). In these sediments, CSB form cm-thick benthic mats that cover tens of thousands of km² of seafloor, from water depths of a few tens of meters to a few hundred meters (Gallardo, 1977; Fossing et al., 1995; Jørgensen and Gallardo, 1999).

CSB live at the oxic-anoxic interface, where dissolved H₂S and O₂ or NO₃⁻ coexist in concentrations smaller than 1 μM, or are separated by a small distance of up to a few cm (Teske and Nelson, 2006; Jørgensen, 2010). Laboratory experiments with mats collected from natural environments show that CSB adapt to fluctuating chemical gradients, moving vertically through the sediments and storing dissolved NO₃⁻ and solid S° intracellularly (Fossing et al., 1995; Huettel et al., 1996; Otte et al., 1999; Zopfi et al., 2001; Sayama et al., 2005; Kamp et al., 2006; Preisler et al., 2007; Schutte et al., 2018). When bottom waters are forced to be anoxic, CSB filaments protrude from the sediment, internal stores of NO₃⁻ are reduced with ambient dissolved H₂S (Fossing et al., 1995; Otte et al., 1999; Sayama et al., 2005), and oxidized H₂S is stored internally as solid S°. Then, when bottom waters are forced to be oxic, CSB filaments retreat into the sediment, and internal S° stores are oxidized to SO₄²⁻ using bottom water dissolved O₂ or NO₃⁻. This metabolic flexibility, together with the vertical motility of filaments, allow CSB to support energy-yielding metabolism for days to months even if electron donors and acceptors are physically separated.

In the field, the use of internal NO₃⁻ stores to oxidize H₂S has been observed and quantified by benthic biogeochemical studies of shelf sediments offshore Peru (Dale et al., 2016; Sommer et al., 2016). To our knowledge, the quantitative field observation of CSB thriving on oxidation of internal S° stores while oxidizing bottom water O₂ or NO₃⁻ has not been made yet. Based on the interpretation of the fossil filaments as CSB, on the evidence for intense but

intermittent biogeochemical activity in marginal basins and on the knowledge of CSB metabolism, in the next section we fully develop the scenario of biogeochemical low-salinity gypsum formation (Fig. 8, Table 3) that applies principally to the filament-bearing vertically oriented bottom-grown crystals (Fig. 7) of the Primary Lower Gypsum unit.

6.5.3 Low-salinity gypsum precipitation promoted by the biogeochemical S cycle

Our scenario for the involvement of the biogeochemical sulfur cycle in the formation of low-salinity gypsum (Fig. 8; Table 3) relies on the evidence cited above that the deposition of the Primary Lower Gypsum unit was influenced by (i) precession driven climate change, recorded by lithological cycles composed of marls/gypsum couplets (Krijgsman et al., 1999), and (ii) shorter term, seasonal/annual cycles that produced the lamination in the selenite crystals of the gypsum layers (Dela Pierre et al., 2015; Reghizzi et al., 2018). Refer to Table 4 for the stoichiometry of numbered biogeochemical processes in the text that follows.

Marls were deposited during minima of precession, and thus maxima of insolation, when the hydrological cycle is enhanced and marginal basins received the highest fluxes of continental runoff (Lugli et al., 2010; Topper et al., 2014; Dela Pierre et al., 2014; Reghizzi et al., 2018). In these hydrological conditions, intense continental runoff kept the water column permanently stratified throughout the annual cycle. Stratification limited the transport of nutrients from the deep waters to surface waters; NO_3^- in the surface water was depleted, and N_2 -fixation (diazotrophy, process 1) dominated primary productivity. In deep waters, degradation of settling marine snow (process 3) released nutrients that built-up in the dissolved form. Marine snow that escaped degradation accumulated on the seafloor leading to organic-matter rich marls. Water column stratification also limited the transport of surface dissolved O_2 into deep waters, resulting in decreased deep water O_2 concentrations and, eventually, bottom water anoxia that enhanced organic matter preservation. At the chemocline separating surface oxic from deep anoxic waters, pelagic communities of anoxygenic phototrophic bacteria (process 2) developed. At the benthic boundary, CSB mats thrived by using bottom water NO_3^- to oxidize H_2S (process 4) produced by sulfate reduction (process 5) in the underlying organic-matter rich, sulfidic sediments, in a process known as dissimilatory nitrate reduction to ammonium (DNRA). While thriving on this catabolic metabolism, CSB stored solid S° intracellularly (process 4).

Gypsum was deposited at precession maxima (insolation minima) when the average intensity of the hydrological cycle decreased, and the intensity and duration of seasonal aridity was enhanced, driving vertical mixing events in the water column on a yearly basis. Vertical water

column mixing transported nutrients from the deep-water column to surface waters, enhancing surface NO_3^- -based, possibly diatom-dominated, primary productivity (process 6), while surface O_2 was mixed in bottom waters producing a seasonal event of bottom water oxygenation and aerobic organic matter degradation (process 7). Oxygenated bottom water conditions resulted in a switch of metabolic strategy from DRNA ($\text{H}_2\text{S} \Rightarrow \text{S}^\circ$) to oxidation of S° to SO_4^{2-} using bottom water O_2 and/or NO_3^- (process 9). Inside the diffusion-limited CSB mat, SO_4^{2-} production resulted in a dissolved SO_4^{2-} peak, producing gypsum supersaturation and the precipitation of a mm-thick gypsum lamina that rapidly entrapped the biogenic material (filaments, marine snow, diatoms) (process 10). Gypsum precipitation was possibly enhanced by the production of dissolved Ca^{2+} within the mat via dissolution of settled planktonic CaCO_3 skeletons (e.g. planktic foraminifers, coccolithophores) (process 8) driven by the acidity produced during S° conversion to SO_4^{2-} (process 9). This hypothesis is supported by the fact that only siliceous microfossils (diatoms) are preserved in gypsum (Carnevale et al., 2019; Pellegrino et al., 2021), suggesting that the absence of biogenic calcite can reflect a diagenetic bias (Dela Pierre et al., 2014).

During precession maxima, seasonal water column mixing events took place during the arid season, alternated with periods of water column stratification during the humid season, when the marginal basin behaved in a similar way to what happened during precession minima (see above). The rapid rate (hours) at which benthic mats respond to changes in bottom water chemistry in laboratory experiments (Fossing et al., 1995; Huettel et al., 1996; Otte et al., 1999; Zopfi et al., 2001; Sayama et al., 2005; Kamp et al., 2006; Preisler et al., 2007), makes this hypothesized seasonal shift between S° storage and S° oxidation to SO_4^{2-} plausible.

The biogeochemical scenario for low-salinity gypsum formation has to be tested against the $\delta^{34}\text{S}$ and $\delta^{18}\text{O}$ of gypsum deposits (Fig. 3). More than 80% of the $\delta^{34}\text{S}_{\text{SO}_4}$ values of dissolved SO_4^{2-} are included within a very narrow range, from 21 to 23 ‰ vs CDT (Fig. 3), centered around the Messinian oceanic dissolved sulfate $\delta^{34}\text{S}$ composition (~ 22 ‰ vs CDT; Masterson et al., 2016). This seems to be at odds with the existence of a dynamic biogeochemical S cycle, because sulfate reduction discriminates strongly against dissolved $^{34}\text{SO}_4^{2-}$ (Canfield, 2001; Detmers et al., 2001; Bruchert et al., 2001; Habicht et al., 2002; Canfield et al., 2006; Sim et al., 2011), and other processes of the S cycle impart supplementary fractionation to dissolved sulfur species (Canfield et al., 1998; Habicht et al., 1998; Bottcher et al., 2001; Zerkle et al., 2009; Pellerin et al., 2019; Findlay et al., 2019).

Nevertheless, the invariant $\delta^{34}\text{S}_{\text{SO}_4}$ could be due to an efficient microbial re-oxidation of H_2S to SO_4^{2-} via S° within the CSB mat. The mat exchanges sulfur uniquely via diffusive influx of SO_4^{2-} from bottom waters and loss of SO_4^{2-} via gypsum precipitation, while the sink via the precipitation of solid sulfides is negligible (the average reduced S concentration in the Vena del Gesso gypsum, for example, is < 170 ppm, data not shown). In these conditions, the $\delta^{34}\text{S}$ of the SO_4^{2-} sink (gypsum precipitation) must be equal to the $\delta^{34}\text{S}$ of the SO_4^{2-} source (diffusion of SO_4^{2-} from bottom waters). Evidence exists from a variety of organic-rich sedimentary environments that the efficient anaerobic oxidation of H_2S to SO_4^{2-} , known as the “cryptic sulfur cycle”, indeed results in a zone of constant $\delta^{34}\text{S}_{\text{SO}_4}$ of dissolved SO_4 with sediment depth (Aller et al., 2010; Mills et al., 2016; Antler et al., 2019).

The $\delta^{18}\text{O}$ values of dissolved sulfate deduced from analyses of gypsum (Fig. 3) show a larger range, from 6 to 15 ‰ vs SMOW. Bacterial sulfate reduction discriminates against ^{18}O -bearing dissolved SO_4^{2-} , resulting in an increase in $\delta^{18}\text{O}$ of residual sulfate as sulfate reduction proceeds (Brunner et al., 2005; Antler et al., 2013). In addition to this effect, intracellular oxidation of the sulfite (SO_3^{2-}) intermediate to sulfate, and the excretion of the newly produced sulfate to the extracellular domain, introduces oxygen isotopes from water in the dissolved sulfate pool (Mizutani and Rafter, 1973; Fritz et al., 1989; Wortmann et al., 2007; Farquhar et al., 2008; Turchyn et al., 2010; Brunner et al., 2012; Kohl et al., 2012; Antler et al., 2013). Further, oxygen from water molecules is introduced in the dissolved sulfate pool during the re-oxidation of H_2S (Jørgensen, 1990; Thamdrup et al., 1994; Canfield et al., 1998, 2005; Kamyshny and Ferkelman, 2010). As a result, in sediments characterized by efficient re-oxidation of H_2S to SO_4^{2-} , $\delta^{18}\text{O}_{\text{SO}_4}$ is strongly influenced by the $\delta^{18}\text{O}$ of ambient waters (Aller et al., 2010; Mills et al., 2016; Blonder et al., 2017).

Considering that the marginal basin where Primary Lower Gypsum and Upper Gypsum deposits formed had a range of $\delta^{18}\text{O}_{\text{H}_2\text{O}}$ values (Fig. 2), it is not surprising that, in the face of a quasi-constant $\delta^{34}\text{S}_{\text{SO}_4}$, the $\delta^{18}\text{O}$ values of dissolved sulfate show a range of about 9 ‰ vs SMOW (Fig. 3). In support of this interpretation, the gypsum deposits from the Eraclea Miona section, that have the highest $\delta^{18}\text{O}_{\text{SO}_4}$ values, are also those that have highest $\delta^{18}\text{O}_{\text{H}_2\text{O}}$ (Fig. 2b). In summary, the $\delta^{34}\text{S}_{\text{SO}_4}$ and $\delta^{18}\text{O}_{\text{SO}_4}$ compositions of Messinian Salinity Crisis low-salinity gypsum deposits are consistent with an efficient H_2S re-oxidation in waters of variable $\delta^{18}\text{O}_{\text{H}_2\text{O}}$ within the CSB mat.

Given that CSB mats cover vast portions of continental margin sediments overlain by highly-productive and intermittently anoxic water columns (Jørgensen, 1977; Gallardo, 1977; Mussmann et al., 2003), why doesn't gypsum precipitate in these modern settings? The answer might lie in that these modern systems are less biogeochemically dynamic compared to those that promoted the formation of low salinity gypsum during the Messinian Salinity Crisis. For example, an 11 years long biogeochemical study of water column and benthic biogeochemical processes on the Peru margin (Graco et al., 2001; Dale et al., 2017) showed that sediments were anoxic throughout this multi-annual period, bottom water O_2 varied between 0 and 10 $\mu\text{mol litre}^{-1}$, while NO_3^- concentrations varied between 0 and 20 $\mu\text{mol litre}^{-1}$. In these conditions, benthic CSB communities are forced in the DRNA metabolic mode whereby they use internal NO_3^- stores to oxidize sedimentary H_2S to S^0 . No field evidence of the alternative growth mode ($\text{S}^0 \Rightarrow \text{SO}_4^{2-}$) was observed. Further, if anoxic bottom water conditions persist, and degradation of phytodetritus accumulating at the seafloor is intense, then the H_2S flux from below can outcompete the oxidative ability of CSB, the internal NO_3^- stores can be depleted and the CSB mats are destroyed (Sommer et al., 2016). The Peru mats investigated to date seem to live at the boundary between the DRNA metabolic strategy and being overwhelmed by the benthic H_2S flux. In summary, the laboratory-observed rapid switching between the two metabolic strategies that CSB are capable of - that is one of the bases of our biogeochemical scenario of low-salinity gypsum formation - is not taking place on the Peru margin.

In summary, we propose that the biogeochemical sulfur cycle did not act alone to produce gypsum saturation, but was one of at least three factors that include the prevailing evaporative conditions and, possibly, Ca^{2+} - and SO_4^{2-} -rich continental runoff. The relative importance of biology and Ca^{2+} - and SO_4^{2-} -rich bearing runoff, as opposed to evaporation, dictated the salinity at which gypsum precipitated.

7. Conclusions

In this paper we summarize existing data and present novel geochemical evidence suggesting that gypsum deposits from multiple, geographically separated Mediterranean marginal basins precipitated from low salinity ($S < 110 \text{ g kg}^{-1}$) water masses. The evidence, which is available primarily for Primary Lower Gypsum deposits, comes from (i) the unusually low salinities (mostly $< 50 \text{ g kg}^{-1}$) in gypsum fluid inclusions from the Sorbas basin (Spain), the Catanzaro

Trough (southern Italy), the Vena del Gesso basin (northern Italy) and the Piedmont basin (northern Italy); and (ii) unusually light oxygen isotope composition ($\delta^{18}\text{O} < 0\ \text{\textperthousand}$ vs SMOW) of gypsum parent waters from the Piedmont basin (northern Italy) and the Sorbas basin (Spain). We propose that multiple factors, including evaporative conditions, Ca^{2+} - and SO_4^{2-} -bearing runoff and the biogeochemical sulfur cycle may have acted simultaneously to variable degrees, leading to a span of salinities at gypsum saturation from the thermodynamic value of $110\ \text{g kg}^{-1}$, to salinities lower than modern seawater ($< 35\ \text{g kg}^{-1}$). The involvement of biogeochemistry, via the production of a microbially-mediated, and temporally transient, increase of dissolved sulfate in a CSB-dominated benthic microbial mat, is suggested by independent petrographic and organic geochemical evidence. Should our scenario for the formation of low-salinity gypsum be confirmed for other geological epochs, it would imply that large gypsum deposits do not require evaporation to increase seawater salinity in excess of $110\ \text{g kg}^{-1}$, expanding the range of environments that promote marine gypsum deposition. It would also imply that an additional, biological coupling between the calcium, sulfur and carbon cycles exists.

Acknowledgements

We thank Felice Tirabasso and Matthias Reiman (Knauf) for granting access and permission to sample the Castellina Marittima quarry (Tuscany, Italy). We thank Stefano Marabini and Saint Gobain for granting access and permission to sample the Monte Tondo quarry (Vena del Gesso, Italy). We thank Christophe Thomazo for carrying out the $\delta^{18}\text{O}_{\text{SO}_4}$ analyses at the Université de Bourgogne (Dijon). This work was supported by the French TELLUS-Marges program and by the European Union's Horizon 2020 research and innovation programme under the Marie Skłodowska-Curie grant agreement No 765256 (ETN SaltGiant). This work benefitted from very useful comments provided by two anonymous reviewers.

Appendix A. Supplementary material

References

- Aller R. C., Madrid V., Chistoserdov A., Aller J. Y. and Heilbrun C. (2010) Unsteady diagenetic processes and sulfur biogeochemistry in tropical deltaic muds: Implications for oceanic isotope cycles and the sedimentary record. *Geochim. Cosmochim. Acta* **74**, 4671–4692.

- Andreetto F., Aloisi G., Raad F., Heida H., Flecker R., Agiadi K., Lofi J., Blondel S., Bulian F., Camerlenghi A., Caruso A., Ebner R., Garcia-Castellanos D., Gaullier V., Guibourdenche L., Gvirtzman Z., Hoyle T. M., Meijer P. T., Moneron J., Sierro F. J., Travani G., Tzehavirtzman A., Vasiliev I. and Krijgsman W. (2021) Freshening of the Mediterranean Salt Giant: controversies and certainties around the terminal (Upper Gypsum and Lago-Mare) phases of the Messinian Salinity Crisis. *Earth-Sci. Rev.* **216**, 103577.
- Antler G., Mills J. V., Hutchings A. M., Redeker K. R. and Turchyn A. V. (2019) The Sedimentary Carbon-Sulfur-Iron Interplay – A Lesson From East Anglian Salt Marsh Sediments. *Front. Earth Sci.* **7**, 140.
- Antler G., Turchyn A. V., Rennie V., Herut B. and Sivan O. (2013) Coupled sulfur and oxygen isotope insight into bacterial sulfate reduction in the natural environment. *Geochim. Cosmochim. Acta* **118**, 98–117.
- Archer C. L. (2005) Evaluation of global wind power. *J. Geophys. Res.* **110**, D12110.
- Artiaga D., Garcia-Veigas J., Cendon D. I., Atalar C. and Gibert L. (2021) The Messinian evaporites of the Mesaoria basin (North Cyprus): A discrepancy with the current chronostratigraphic understanding. *Palaeogeogr. Palaeoclimatol. Palaeoecol.* **584**, 110681.
- Attia O. E., Lowenstein T. K. and Wali A. M. A. (1995) Middle Miocene gypsum, Gulf of Suez: Marine or nonmarine ? *J. Sediment. Res.* **A65**, 614–626.
- Ayora C., Taberner C., Pierre C. and Pueyo J.-J. (1995) Modeling the sulfur and oxygen isotopic composition of sulfates through a halite-potash sequence: Implications for the hydrological evolution of the Upper Eocene Southpyrenean Basin. *Geochim. Cosmochim. Acta* **59**, 1799–1808.
- van Baak C., Krijgsman W., Magyar I., Sztano O., Golovina L., Grothe A., Hoyle T., Mandic O., Patina I., Popov S., Radionova E., Stoica M. and Vasiliev I. (2017) Paratethys response to the Messinian salinity crisis. *Earth-Sci. Rev.* **172**, 193–223.
- Babel M. and Schreiber B. C. (2014) Geochemistry of Evaporites and Evolution of Seawater. In *Treatise on Geochemistry (Second Edition)* (eds. H. D. Holland and K. K. Turekian). Elsevier, Oxford. pp. 483–560.
- Bath A. H., Darling W. G., George I. A. and Mildowski A. E. (1987) $^{18}\text{O}/^{16}\text{O}$ and $^{2}\text{H}/^{1}\text{H}$ changes during progressive hydration of a Zechstein anhydrite formation. *Geochim. Cosmochim. Acta* **51**, 3113–3118.
- Benetti M., Reverdin G., Aloisi G. and Sveinbjornsdottir A. (2017a) Stable isotopes in surface waters of the Atlantic Ocean: Indicators of ocean-atmosphere water fluxes and oceanic mixing processes. *J. Geophys. Res.-Oceans* **122**, 4723–4742.
- Benetti M., Steen-Larsen H. C., Reverdin G., Sveinbjornsdottir A. E., Aloisi G., Berkelhammer M. B., Bourles B., Bourras D., de Coetlogon G., Cosgrove A., Faber A. K., Grelet J.,

Hansen S. B., Johnson R., Legoff H., Martin N., Peters A. J., Popp T. J., Reynaud T. and Winther M. (2017b) Stable isotopes in the atmospheric marine boundary layer water vapour over the Atlantic Ocean, 2012–2015. *Sci Data* **4**, 160128.

Berner E. K. and Berner R. A. (2012) *Global Environment: Water, Air and Geochemical Cycles*. 2nd ed., Princeton University Press.

Bigi D., Lugli S., Manzi V. and Roveri M. (2022) Are fluid inclusions in gypsum reliable paleoenvironmental indicators? An assessment of the evidence from the Messinian evaporites. *Geology*.

Blonder B., Boyko V., Turchyn A. V., Antler G., Sinichkin U., Knossow N., Klein R. and Kamysny A. (2017) Impact of Aeolian Dry Deposition of Reactive Iron Minerals on Sulfur Cycling in Sediments of the Gulf of Aqaba. *Front. Microbiol.* **8**, 1131.

Bodnar R. (1993) Revised Equation and Table for Determining the Freezing-Point Depression of H₂O-NaCl Solutions. *Geochim. Cosmochim. Acta* **57**, 683–684.

Bottcher M. E., Thamdrup B. and Vennemann T. W. (2001) Oxygen and sulfur isotope fractionation during anaerobic bacterial disproportionation of elemental sulfur. *Geochim. Cosmochim. Acta* **65**, 1601–1609.

Braitsch O. (1971) *Salt Deposits, Their Origin and Composition*., Springer-Verlag, New York.

Brand W. A., Coplen T. B., Vogl J., Rosner M. and Prohaska T. (2014) Assessment of international reference materials for isotope-ratio analysis (IUPAC Technical Report). *Pure Appl. Chem.* **86**, 425–467.

Brass G. W. (1976) The variation of the marine ⁸⁷Sr/⁸⁶Sr ratio during the Phanerozoic time: interpretation using a flux model. *Geochim. Cosmochim. Acta* **40**, 721–730.

Bruchert V., Knoblauch C. and Jorgensen B. B. (2001) Controls on stable sulfur isotope fractionation during bacterial sulfate reduction in Arctic sediments. *Geochim. Cosmochim. Acta* **65**, 763–776.

Brunner B., Bernasconi S. M., Kleikemper J. and Schroth M. H. (2005) A model for oxygen and sulfur isotope fractionation in sulfate during bacterial sulfate reduction processes. *Geochim. Cosmochim. Acta* **69**, 4773–4785.

Brunner B., Einsiedl F., Arnold G. L., Müller I., Templer S. and Bernasconi S. M. (2012) The reversibility of dissimilatory sulphate reduction and the cell-internal multi-step reduction of sulphite to sulphide: insights from the oxygen isotope composition of sulphate. *Isotopes Environ. Health Stud.* **48**, 33–54.

Burke A., Present T. M., Paris G., Rae E. C. M., Sandilands B. H., Gaillardet J., Peucker-Ehrenbrink B., Fischer W. W., McClelland J. W., Spencer R. G. M., Voss B. M. and Adkins J. F. (2018) Sulfur isotopes in rivers: Insights into global weathering budgets, pyrite oxidation, and the modern sulfur cycle. *Earth Planet. Sci. Lett.* **496**, 168–177.

- Callbeck C. M., Canfield D. E., Kuypers M. M. M., Yilmaz P., Lavik G., Thamdrup B., Schubert C. J. and Bristow L. A. (2021) Sulfur cycling in oceanic oxygen minimum zones. *Limnol. Oceanogr.*, 11759.
- Canfield D. E. (2001) Biogeochemistry of sulfur isotopes. *Stable Isot. Geochem.* **43**, 607–636.
- Canfield D. E., Kristensen E. and Thamdrup B. (2005) The sulfur cycle. In *Aquatic Geomicrobiology* Academic Press Ltd-Elsevier Science Ltd, London. pp. 313–381.
- Canfield D. E., Olesen C. A. and Cox R. P. (2006) Temperature and its control of isotope fractionation by a sulfate-reducing bacterium. *Geochim. Cosmochim. Acta* **70**, 548–561.
- Canfield D. E., Thamdrup B. and Fleischer S. (1998) Isotope fractionation and sulfur metabolism by pure and enrichment cultures of elemental sulfur-disproportionating bacteria. *Limnol. Oceanogr.* **43**, 253–264.
- Carnevale G., Gennari R., Lozar F., Natalicchio M., Pellegrino L. and Dela Pierre F. (2019) Living in a deep desiccated Mediterranean Sea: An overview of the Italian fossil record of the Messinian salinity crisis. *Boll. Della Soc. Paleontol. Ital.* **58**, 109–140.
- Caruso A., Pierre C., Blanc-Valleron M. and Rouchy J. (2015) Carbonate deposition and diagenesis in evaporitic environments: The evaporative and sulphur-bearing limestones during the settlement of the Messinian Salinity Crisis in Sicily and Calabria. *Palaeogeogr. Palaeoclimatol. Palaeoecol.* **429**, 136–162.
- Cendón D. I., Peryt T. M., Ayora C., Pueyo J. J. and Taberner C. (2004) The importance of recycling processes in the Middle Miocene Badenian evaporite basin (Carpathian foredeep): palaeoenvironmental implications. *Palaeogeogr. Palaeoclimatol. Palaeoecol.* **212**, 141–158.
- CIESM (2008) *The Messinian Salinity Crisis from mega deposits to microbiology. A consensus report.*, Monaco.
- Clauer N., Chaudhuri S., Toulkeridis T. and Blanc G. (2000) Fluctuations of Caspian Sea level: Beyond climatic variations ? *Geology* **28**, 1015–1018.
- Cosentino D., Bracone V., D'Amico C., Cipollari P., Esu D., Faranda C., Frezza V., Gliozzi E., Grossi F., Guerrieri P., Iadanza A., Kotsakis T. and Soulie-Marsche I. (2018) The record of the Messinian salinity crisis in mobile belts: Insights from the Molise allochthonous units (southern Apennines, Italy). *Palaeogeogr. Palaeoclimatol. Palaeoecol.* **503**, 112–130.
- Costanzo A., Cipriani M., Feely M., Cianflone G. and Dominici R. (2019) Messinian twinned selenite from the Catanzaro Trough, Calabria, Southern Italy: field, petrographic and fluid inclusion perspectives. *Carbonates Evaporites* **34**, 743–756.
- Craig H. and Gordon L. I. (1965) Deuterium and oxygen 18 variations in the ocean and the marine atmosphere. In *Stable Isotopes in oceanographic studies and*

paleotemperatures (ed. E. Tongiorgi). Consiglio Nazionale delle Richerche, Pisa. pp. 9–130.

Dale A. W., Graco M. and Wallmann K. (2017) Strong and Dynamic Benthic-Pelagic Coupling and Feedbacks in a Coastal Upwelling System (Peruvian Shelf). *Front. Mar. Sci.* **4**, 29.

Dale A. W., Sommer S., Lomnitz U., Bourbonnais A. and Wallmann K. (2016) Biological nitrate transport in sediments on the Peruvian margin mitigates benthic sulfide emissions and drives pelagic N loss during stagnation events. *Deep Sea Res. Part Oceanogr. Res. Pap.* **112**, 123–136.

Dela Pierre F., Bernardi E., Cavagna S., Clari P., Gennari R., Irace A., Lozar F., Lugli S., Manzi V., Natalicchio M., Roveri M. and Violanti D. (2011) The record of the Messinian salinity crisis in the Tertiary Piedmont Basin (NW Italy): The Alba section revisited. *Palaeogeogr. Palaeoclimatol. Palaeoecol.* **310**, 238–255.

Dela Pierre F., Clari P., Bernardi E., Natalicchio M., Costa E., Cavagna S., Lozar F., Lugli S., Manzi V., Roveri M. and Violanti D. (2012) Messinian carbonate-rich beds of the Tertiary Piedmont Basin (NW Italy): Microbially-mediated products straddling the onset of the salinity crisis. *Palaeogeogr. Palaeoclimatol. Palaeoecol.* **344**, 78–93.

Dela Pierre F., Clari P., Natalicchio M., Ferrando S., Giustetto R., Lozar F., Lugli S., Manzi V., Roveri M. and Violanti D. (2014) Flocculent layers and bacterial mats in the mudstone interbeds of the Primary Lower Gypsum unit (Tertiary Piedmont basin, NW Italy): Archives of palaeoenvironmental changes during the Messinian salinity crisis. *Mar. Geol.* **355**, 71–87.

Dela Pierre F., Natalicchio M., Ferrando S., Giustetto R., Birgel D., Carnevale G., Gier S., Lozar F., Marabbello D. and Peckmann J. (2015) Are the large filamentous microfossils preserved in Messinian gypsum colorless sulfide-oxidizing bacteria? *Geology* **43**, 855–858.

Delattre H., Vallet-Coulomb C. and Sonzogni C. (2015) Deuterium excess in the atmospheric water vapour of a Mediterranean coastal wetland: regional vs. local signatures. *Atmospheric Chem. Phys.* **15**, 10167–10181.

Detmers J., Bruchert V., Habicht K. S. and Kuever J. (2001) Diversity of sulfur isotope fractionations by sulfate-reducing prokaryotes. *Appl. Environ. Microbiol.* **67**, 888–894.

Driussi O., Maillard A., Ochoa D., Lofi J., Chanier F., Gaullier V., Briais A., Sage F., Sierro F. and Garcia M. (2015) Messinian Salinity Crisis deposits widespread over the Balearic Promontory: Insights from new high-resolution seismic data. *Mar. Pet. Geol.* **66**, 41–54.

Eickhoff M., Birgel D., Talbot H. M., Peckmann J. and Kappler A. (2013) Oxidation of Fe(II) leads to increased C-2 methylation of pentacyclic triterpenoids in the anoxygenic phototrophic bacterium *Rhodopseudomonas palustris* strain TIE-1. *Geobiology* **11**, 268–278.

- Evans N., Turchyn A., Gazquez F., Bontognali T., Chapman H. and Hodell D. (2015) Coupled measurements of delta O-18 and delta D of hydration water and salinity of fluid inclusions in gypsum from the Messinian Yesares Member, Sorbas Basin (SE Spain). *Earth Planet. Sci. Lett.* **430**, 499–510.
- Farquhar J., Canfield D. E., Masterson A., Bao H. and Johnston D. (2008) Sulfur and oxygen isotope study of sulfate reduction in experiments with natural populations from Faellestrand, Denmark. *Geochim. Cosmochim. Acta* **72**, 2805–2821.
- Findlay A. J., Boyko V., Pellerin A., Ayetisyan K., Guo Q., Yang X. and Kamyshny A. (2019) Sulfide oxidation affects the preservation of sulfur isotope signals. *Geology* **47**, 739–743.
- Flecker R., de Villiers S. and Ellam R. (2002) Modelling the effect of evaporation on the salinity-Sr-87/Sr-86 relationship in modern and ancient marginal-marine systems: the Mediterranean Messinian Salinity Crisis. *Earth Planet. Sci. Lett.* **203**, 221–233.
- Fontes J.-C. (1966) Fractionnement isotopique dans l'eau de cristallisation du sulfate de calcium. *Geol. Rundsch.* **55**, 172–178.
- Fontes J.-C. and Gonfiantini R. (1967) Fractionnement isotopique de l'hydrogène dans l'eau de cristallisation du gypse. *Comptes Rendus L'Academie Sci. Paris* **265**, 4–6.
- Fossing H., Gallardo V., Jorgensen B., Huttel M., Nielsen L., Schulz H., Canfield D., Forster S., Glud R., Gundersen J., Kuver J., Ramsing N., Teske A., Thamdrup B. and Ulloa O. (1995) Concentration and Transport of Nitrate by the Mat-Forming Sulfur Bacterium Thioploca. *Nature* **374**, 713–715.
- Fotherby A., Bradbury H. J., Antler G., Sun X., Druhan J. L. and Turchyn A. V. (2021) Modelling the Effects of Non-Steady State Transport Dynamics on the Sulfur and Oxygen Isotope Composition of Sulfate in Sedimentary Pore Fluids. *Front. Earth Sci.* **8**, 587085.
- Fritz P., Basharmal G. M., Drimmie R. J., Ibsen J. and Qureshi R. M. (1989) Oxygen isotope exchange between sulphate and water during bacterial reduction of sulphate. *Chem. Geol. Isot. Geosci. Sect.* **79**, 99–105.
- Gaillardet J., Dupré B., Louvat P. and Allègre C. J. (1999) Global silicate weathering and CO₂ consumption rates deduced from the chemistry of large rivers. *Chem. Geol.* **159**, 3–30.
- Gallardo V. A. (1977) Large benthic microbial communities in sulphide biota under Peru–Chile Subsurface Countercurrent. *Nature* **268**, 331–332.
- Gallardo V. A., Klingelhoeffer E., Arntz W. and Graco M. (1998) First Report of the Bacterium Thioploca in the Benguela Ecosystem off Namibia. *J. Mar. Biol. Assoc. U. K.* **78**, 1007–1010.

- Garcia-Veigas J., Cendon D., Gibert L., Lowenstein T. and Artiaga D. (2018) Geochemical indicators in Western Mediterranean Messinian evaporites: Implications for the salinity crisis. *Mar. Geol.* **403**, 197–214.
- Garcia-Veigas J., Gibert L., Cendon D., Artiaga D., Corbi H., Soria J., Lowenstein T. and Sanz E. (2020) Late Miocene evaporite geochemistry of Lorca and Fortuna basins (Eastern Betics, SE Spain): Evidence of restriction and continentalization. *Basin Res.* **32**, 926–958.
- Gat J. R., Klein B., Kushnir Y., Roether W., Wernli H., Yam R. and Shemesh A. (2003) Isotope composition of air moisture over the Mediterranean Sea: an index of the air-sea interaction pattern. *Tellus B Chem. Phys. Meteorol.* **55B**, 953–965.
- Gazquez F., Evans N. P. and Hodell D. A. (2017) Precise and accurate isotope fractionation factors (δ O-17, δ O-18 and δ D) for water and $\text{CaSO}_4 \cdot 2\text{H}_2\text{O}$ (gypsum). *Geochim. Cosmochim. Acta* **198**, 259–270.
- Geng L., Savarino J., Savarino C. A., Caillon N., Cartigny P., Hattori S., Ishino S. and Yoshida N. (2018) A simple and reliable method reducing sulfate to sulfide for multiple sulfur isotope analysis. *Rapid Commun. Mass Spectrom.* **32**, 333–341.
- Gerstenberger H., Haase G. and Nour F. A. E. (1997) The Origin of Strontium and the Strontium Isotope Budget of the River Nile. *Isotopes Environ. Health Stud.* **33**, 349–356.
- Giustini F., Brilli M. and Patera A. (2016) Mapping oxygen stable isotopes of precipitation in Italy. *J. Hydrol. Reg. Stud.* **8**, 162–181.
- Goldstein R. H. and Reynolds T. J. (1994) *Systematics of Fluid Inclusions in Diagenetic Minerals.*, Society for Sedimentary Geology, Tulsa, Oklahoma, USA.
- Graco M., Farias L., Molina V., Gutierrez D. and Nielsen L. P. (2001) Massive developments of microbial mats following phytoplankton blooms in a naturally eutrophic bay: Implications for nitrogen cycling. *Limnol. Oceanogr.* **46**, 821–832.
- Grothe A., Andreetto F., Reichart G.-J., Wolthers M., Van Baak C. G. C., Vasiliev I., Stoica M., Sangiorgi F., Middelburg J. J., Davies G. R. and Krijgsman W. (2020) Paratethys pacing of the Messinian Salinity Crisis: Low salinity waters contributing to gypsum precipitation? *Earth Planet. Sci. Lett.* **532**, 116029.
- Grothe A., Sangiorgi F., Mulders Y., Vasiliev I., Reichart G., Brinkhuis H., Stoica M. and Krijgsman W. (2014) Black Sea desiccation during the Messinian Salinity Crisis: Fact or fiction? *Geology* **42**, 563–566.
- Habicht K. S., Canfield D. E. and Rethmeier J. (1998) Sulfur isotope fractionation during bacterial reduction and disproportionation of thiosulfate and sulfite. *Geochim. Cosmochim. Acta* **62**, 2585–2595.

- Habicht K. S., Gade M., Thamdrup B., Berg P. and Canfield D. E. (2002) Calibration of sulfate levels in the Archean Ocean. *Science* **298**, 2372–2374.
- Halevy I., Peters S. and Fischer W. (2012) Sulfate Burial Constraints on the Phanerozoic Sulfur Cycle. *Science* **337**, 331–334.
- Hall D. and Stern S. (1993) Preferential Water-Loss from Synthetic Fluid Inclusions. *Contrib. Mineral. Petrol.* **114**, 489–500.
- Hansen K. W. and Wallmann K. (2003) Cretaceous and Cenozoic evolution of seawater composition, atmospheric O₂ and CO₂: a model perspective. *Am. J. Sci.* **303**, 94–148.
- Haq B., Gorini C., Baur J., Moneron J. and Rubino J. (2020) Deep Mediterranean's Messinian evaporite giant: How much salt? *Glob. Planet. Change* **184**.
- Hardie A. H. (1996) Secular variation in seawater chemistry: An explanation for the coupled secular variation in the mineralogies of marine limestones and potash evaporites over the past 600 m.y. *Geology* **24**, 279–283.
- Hardie L. A. (1984) Evaporites: Marine or Non-Marine. *Am. J. Sci.* **284**, 193–240.
- Harvie C. E. and Weare J. H. (1980) The prediction of mineral solubilities in natural waters: the Na-K-Mg-Ca-Cl-SO₄-H₂O system from zero to high concentrations at 25°C. *Geochim. Cosmochim. Acta* **44**, 981–997.
- Harvie C. E., Weare J. H., Hardie L. A. and Eugster H. P. (1980) Evaporation of Seawater: Calculated Mineral Sequences. *Science* **208**, 498–500.
- Herrmann A. G., Knake D., Schneider J. and Peters H. (1973) Geochemistry of modern seawater and brines from salt pans: main components and bromine distributions. *Contr. Mineral. Petrol.* **40**, 1–24.
- Hsü K. J., Ryan W. B. F. and Cita M. B. (1973) Late Miocene Desiccation of the Mediterranean. *Nature* **242**, 240–244.
- Huettel M., Forster S., Kloster S. and Fossing H. (1996) Vertical Migration in the Sediment-Dwelling Sulfur Bacteria Thioploca spp. in Overcoming Diffusion Limitations. *Appl. Environ. Microbiol.* **62**, 1863–1872.
- IAEA (2005) *Isotopic composition of precipitation in the Mediterranean Basin in relation to air circulation patterns and climate.*, International Atomic Energy Agency.
- Isaji Y., Kawahata H., Takano Y., Ogawa N., Kuroda J., Yoshimura T., Lugli S., Manzi V., Roveri M. and Ohkouchi N. (2019) Diazotrophy Drives Primary Production in the Organic-Rich Shales Deposited Under a Stratified Environment During the Messinian Salinity Crisis (Vena del Gesso, Italy). *Front. Earth Sci.* **7**, 85.
- Jørgensen B. B. (1990) A Thiosulfate Shunt in the Sulfur Cycle of Marine Sediments. *Science* **249**, 152–154.

- Jørgensen B. B. (2010) Big sulfur bacteria. *ISME J.* **4**, 1083–1084.
- Jorgensen B. B. (1977) Distribution of colorless sulfur bacteria (*Beggiatoa* spp.) in a coastal marine sediment. *Mar. Biol.* **41**, 19–28.
- Jorgensen B. B. and Gallardo V. A. (1999) Thioploca spp: filamentous sulfur bacteria with nitrate vacuoles. *Fems Microbiol. Ecol.* **28**, 301–313.
- Kamp A., Stief P. and Schulz-Vogt H. N. (2006) Anaerobic sulfide oxidation with nitrate by a freshwater *Beggiatoa* enrichment culture. *Appl. Environ. Microbiol.* **72**, 4755–4760.
- Kamyshny A. and Ferdelman T. G. (2010) Dynamics of zero-valent sulfur species including polysulfides at seep sites on intertidal sand flats (Wadden Sea, North Sea). *Mar. Chem.* **121**, 17–26.
- Kenig F., Damste J., Frewin N., Hayes J. and Deleeuw J. (1995) Molecular Indicators for Paleoenvironmental Change in a Messinian Evaporitic Sequence (vena Del Gesso, Italy). 2. High-Resolution Variations in Abundances and C-13 Contents of Free and Sulfur-bound Carbon Skeletons in a Single Marl Bed. *Org. Geochem.* **23**, 485–526.
- Kleemann G., Poralla K., Englert G., Kjosen H., Liaaenjensen S., Neunlist S. and Rohmer M. (1990) Tetrahymanol from the Phototrophic Bacterium *Rhodopseudomonas-Palustris* - 1st Report of a Gammacerane Triterpene from a Prokaryote. *J. Gen. Microbiol.* **136**, 2551–2553.
- Kohl I. E., Asatryan R. and Bao H. (2012) No oxygen isotope exchange between water and APS-sulfate at surface temperature: Evidence from quantum chemical modeling and triple-oxygen isotope experiments. *Geochim. Cosmochim. Acta* **95**, 106–118.
- Krijgsman W., Blanc-Valleron M., Flecker R., Hilgen F., Kouwenhoven T., Merle D., Orszag-Sperber F. and Rouchy J. (2002) The onset of the Messinian salinity crisis in the Eastern Mediterranean (Pissouri Basin, cyprus). *Earth Planet. Sci. Lett.* **194**, 299–310.
- Krijgsman W., Hilgen F., Raffi I., Sierro F. and Wilson D. (1999) Chronology, causes and progression of the Messinian salinity crisis. *Nature* **400**, 652–655.
- Kroonenberg S. B., Simmons M. D., Alekseevski N. I., Aliyeva E., Allen M. B., Aybulator D. N., Baba-Zadeh A., Badyukova E. N., Davies C., Hinds D. J., Hoogendoorn R. M., Huseynov D., Ibrahimov B., Mamedov P., Overeem I., Rusakov G. V., Suleymanova S., Svitoch A. A. and Vincent S. J. (2005) Two deltas, two basins, one river, one sea. The modern Volga Delta as an analogue of the Neogene Productive Series, South Caspian Basin. In *Special Publications of the Society of Economic Paleontologists and Mineralogists* (eds. L. Giosan and J. P. Bhattacharya). Society of Economic Paleontologists and Mineralogists, Tulsa. pp. 231–256.
- Labidi J., Cartigny P., Birck J. L., Assayag N. and Bourrand J. J. (2012) Determination of multiple sulfur isotopes in glasses: A reappraisal of the MORB delta S-34. *Chem. Geol.* **334**, 189–198.

- Leavitt W. D., Halevy I., Bradley A. S. and Johnston D. T. (2013) Influence of sulfate reduction rates on the Phanerozoic sulfur isotope record. *Proc. Natl. Acad. Sci.* **110**, 11244–11249.
- Liaaen-Jensen S. (1978) Chemistry of carotenoid pigments. In *The Photosynthetic Bacteria* Plenum Press, New York. pp. 233–247.
- Liotta M., Grassa F., D'Alessandro W., Favara R., Candela E., Pisciotta A. and Scaletta C. (2013) Isotopic composition of precipitation and groundwater in Sicily, Italy. *Appl. Geochem.* **34**, 199–206.
- Lloyd R. (1966) Oxygen Isotope Enrichment of Sea Water by Evaporation. *Geochim. Cosmochim. Acta* **30**, 801–814.
- Lloyd R. M. (1968) Oxygen isotope behavior in the Sulfate-Water System. *J. Geophys. Res.* **1896-1977** **73**, 6099–6110.
- Longinelli A. (1979) Isotope geochemistry of some Messinian evaporites: paleoenvironmental implications. *Palaeogeogr. Palaeoclimatol. Palaeoecol.* **29**, 95–123.
- Lu F. (2006) Lithofacies and water-body record of Messinian evaporites in Nijar Basin, SE Spain. *Sediment. Geol.* **188**, 115–130.
- Lu F. H., Meyers W. J. and Schoonen M. A. (2001) S and O (SO_4) isotopes, simultaneous modeling, and environmental significance of the Nijar messinian gypsum, Spain. *Geochim. Cosmochim. Acta* **65**, 3081–3092.
- Lugli S., Bassetti M. A., Manzi V., Barbieri M., Longinelli A. and Roveri M. (2007) The Messinian ‘Vena del Gesso’ evaporites revisited: characterization of isotopic composition and organic matter. *Geol. Soc. Lond. Spec. Publ.* **285**, 179–190.
- Lugli S., Manzi V., Roveri M. and Schreiber B. (2010) The Primary Lower Gypsum in the Mediterranean: A new facies interpretation for the first stage of the Messinian salinity crisis. *Palaeogeogr. Palaeoclimatol. Palaeoecol.* **297**, 83–99.
- Manzi V., Argnani A., Corcagnani A., Lugli S. and Roveri M. (2020) The Messinian salinity crisis in the Adriatic foredeep: Evolution of the largest evaporitic marginal basin in the Mediterranean. *Mar. Pet. Geol.* **115**, 104288.
- Manzi V., Gennari R., Hilgen F., Krijgsman W., Lugli S., Roveri M. and Sierro F. (2013) Age refinement of the Messinian salinity crisis onset in the Mediterranean. *Terra Nova* **25**, 315–322.
- Manzi V., Gennari R., Lugli S., Roveri M., Scafetta N. and Schreiber B. (2012) High-frequency cyclicity in the Mediterranean Messinian Evaporites: evidence for solar-lunar climate forcing. *J. Sediment. Res.* **82**, 991–1005.
- Manzi V., Lugli S., Roveri M., Dela Pierre F., Gennari R., Lozar F., Natalicchio M., Schreiber B., Taviani M. and Turco E. (2016) The Messinian salinity crisis in Cyprus: a further step

towards a new stratigraphic framework for Eastern Mediterranean. *Basin Res.* **28**, 207–236.

Manzi V., Roveri M., Argnani A., Cowan D. and Lugli S. (2021) Large-scale mass-transport deposits recording the collapse of an evaporitic platform during the Messinian salinity crisis (Caltanissetta basin, Sicily). *Sediment. Geol.* **424**, 106003.

Marzocchi A., Flecker R., van Baak C. G. C., Lunt D. J. and Krijgsman W. (2016) Mediterranean outflow pump: an alternative mechanism for the Lago-mare and the end of the Messinian Salinity Crisis. *Geology* **44**, 523–526.

Masterson A. L., Wing B. A., Paytan A., Farquhar J. and Johnston D. T. (2016) The minor sulfur isotope composition of Cretaceous and Cenozoic seawater sulfate. *Paleoceanography* **31**, 779–788.

McArthur J. M., Howarth R. J. and Bailey T. R. (2001) Strontium Isotope Stratigraphy: LOWESS Version 3: Best fit to the Marine Sr-Isotope curve for 0–509 Ma and accompanying look-up table for deriving numerical age. *J. Geol.* **109**, 155–170.

Meilijson A., Hiigen F., Sepulveda J., Steinberg J., Fairbank V., Fleckere R., Waldmann N., Spaulding S., Bialik O., Boudinot F., Illner P. and Makovsky Y. (2019) Chronology with a pinch of salt: Integrated stratigraphy of Messinian evaporites in the deep Eastern Mediterranean reveals long-lasting halite deposition during Atlantic connectivity. *Earth-Sci. Rev.* **194**, 374–398.

Mekhtieva V. L. and Rabinovich A. L. (1975) Isotope Balance of Sulfur in the Caspian Sea. *Oceanology* **15**, 66–73.

Mills J. V., Antler G. and Turchyn A. V. (2016) Geochemical evidence for cryptic sulfur cycling in salt marsh sediments. *Earth Planet. Sci. Lett.* **453**, 23–32.

Mizutani Y. and Rafter T. (1973) Isotopic behaviour of sulfate oxygen in the bacterial reduction of sulphate. *Geochem. J.* **6**, 183–191.

Mussmann M., Schulz H. N., Strotmann B., Kjær T., Nielsen L. P., Rosselló-Mora R. A., Amann R. I. and Jørgensen B. B. (2003) Phylogeny and distribution of nitrate-storing Beggiatoa spp. in coastal marine sediments. *Environ. Microbiol.* **5**, 523–533.

Natalicchio M., Birgel D., Dela Pierre F., Ziegenbalg S., Hoffmann-Sell L., Gier S. and Peckmann J. (2022) Messinian bottom grown selenitic gypsum: An archive of microbial life. *Geobiology* **20**, 3–21.

Natalicchio M., Birgel D., Peckmann J., Lozar F., Carnevale G., Liu X., Hinrichs K. and Dela Pierre F. (2017) An archaeal biomarker record of paleoenvironmental change across the onset of the Messinian salinity crisis in the absence of evaporites (Piedmont Basin, Italy). *Org. Geochem.* **113**, 242–253.

Natalicchio M., Dela Pierre F., Birgel D., Brumsack H., Carnevale G., Gennari R., Gier S., Lozar F., Pellegrino L., Sabino M., Schnetger B. and Peckmann J. (2019) Paleoenvironmental

change in a precession-paced succession across the onset of the Messinian salinity crisis: Insight from element geochemistry and molecular fossils. *Palaeogeogr. Palaeoclimatol. Palaeoecol.* **518**, 45–61.

Natalicchio M., Dela Pierre F., Lugli S., Lowenstein T., Feiner S., Ferrando S., Manzi V., Roveri M. and Clari P. (2014) Did Late Miocene (Messinian) gypsum precipitate from evaporated marine brines? Insights from the Piedmont Basin (Italy). *Geology* **42**, 179–182.

Natalicchio M., Pellegrino L., Clari P., Pastero L. and Dela Pierre F. (2021) Gypsum lithofacies and stratigraphic architecture of a Messinian marginal basin (Piedmont Basin, NW Italy). *Sediment. Geol.* **425**, 106009.

Ochoa D., Sierro F., Lofi J., Maillard A., Flores J. and Suarez M. (2015) Synchronous onset of the Messinian evaporite precipitation: First Mediterranean offshore evidence. *Earth Planet. Sci. Lett.* **427**, 112–124.

Ogniben L. (1957) Petrografia della serie solfifera siciliana e considerazioni geologiche. *Mem Descr Carta Geol Ital.* **33**, 1–268.

Oliveri E., Neri R., Bellanca A. and Riding R. (2010) Carbonate stromatolites from a Messinian hypersaline setting in the Caltanissetta Basin, Sicily: petrographic evidence of microbial activity and related stable isotope and rare earth element signatures. *Sedimentology* **57**, 142–161.

Ono S., Wing B., Johnston D., Farquhar J. and Rumble D. (2006) Mass-dependent fractionation of quadruple stable sulfur isotope system as a new tracer of sulfur biogeochemical cycles. *Geochim. Cosmochim. Acta* **70**, 2238–2252.

Orti F. (2011) Selenite facies in marine evaporites: A review. *Int. Assoc. Sedimentol. Spec. Publ.* **43**, 431–464.

Otte S., Kuenen J. G., Nielsen L. P., Paerl H. W., Zopfi J., Schulz H. N., Teske A., Strotmann B., Gallardo V. A. and Jorgensen B. B. (1999) Nitrogen, carbon, and sulfur metabolism in natural Thioploca samples. *Appl. Environ. Microbiol.* **65**, 3148–3157.

Palcu D., Vasiliev I., Stoica M. and Krijgsman W. (2019) The end of the Great Khersonian Drying of Eurasia: Magnetostratigraphic dating of the Maeotian transgression in the Eastern Paratethys. *Basin Res.* **31**, 33–58.

Palmer M. R. and Edmond J. M. (1989) The strontium isotope budget of the modern ocean. *Earth Planet. Sci. Lett.* **92**, 11–26.

Panieri G., Lugli S., Manzi V., Roveri M., Schreiber B. and Palinska K. (2010) Ribosomal RNA gene fragments from fossilized cyanobacteria identified in primary gypsum from the late Miocene, Italy. *Geobiology* **8**, 101–111.

Pastor F., Valiente J. A. and Palau J. L. (2017) Sea Surface Temperature in the Mediterranean: Trends and Spatial Patterns (1982–2016). *Pure Appl. Geophys.* **175**, 4017–4029.

- Pellegrino L., Natalicchion M., Abe, K., Jordan, RW, Favero Longo, S., Fernando, S., Carnevale, G., and Dela Pierre, F. (2021) Tiny, glassy and rapidly trapped: the nano-sized planktic diatoms in the Messinian (late Miocene) gypsum. *Geology* **49**.
- Pellerin A., Antler G., Holm S. A., Findlay A. J., Crockford P. W., Turchyn A., Jorgensen B. B. and Finster K. (2019) Large sulfur isotope fractionation by bacterial sulfide oxidation. *Sci. Adv.* **5**, eaaw1480.
- Pierre C. (1982a) Etude isotopique des saumures et des gypses des marais salants de Salin-de-Giraud (Sud de la France). In *Données hydrochimiques, biologiques, isotopiques, sédimentologiques et diagénétiques sur les marais salants de Salin-de-Giraud, Sud de la France* Géologie Méditerranéenne. pp. 479–486.
- Pierre C. (1982b) Teneurs en isotopes stables (^{18}O , ^2H , ^{13}C , ^{34}S) et conditions de génèse des évaporites marines: application à quelques milieux actuels et au Messinien de la Méditerranée. Thèse de doctorat, Université Paris-Sud.
- Pierre C. (2018) The isotopic record of gypsum diagenesis in diluted solutions: Observations in natural salinas and experiments. *Chem. Geol.* **493**, 451–457.
- Playa E., Ortí F. and Rosell L. (2000) Marine to non-marine sedimentation in the upper Miocene evaporites of the Eastern Betics, SE Spain: sedimentological and geochemical evidence. *Sediment. Geol.* **133**, 135–166.
- Preisler A., de Beer D., Lichtschlag A., Lavik G., Boetius A. and Jorgensen B. B. (2007) Biological and chemical sulfide oxidation in a Beggiatoa inhabited marine sediment. *Isme J.* **1**, 341–353.
- Prince J. K. G., Rainbird R. H. and Wing B. A. (2019) Evaporite deposition in the mid-Neoproterozoic as a driver for changes in seawater chemistry and the biogeochemical cycle of sulfur. *Geology* **47**, 375–379.
- Raab M. and Spiro B. (1991) Sulfur isotopic variations during seawater evaporation with fractional crystallization. *Chem. Geol. Isot. Geosci. Sect.* **86**, 323–333.
- Raad F., Lofi J., Mailard A., Tzevahirtzian A. and Caruso A. (2020) The Messinian Salinity Crisis deposits in the Balearic Promontory: An undeformed analog of the MSC Sicilian basins ? *Mar. Pet. Geol.* **124**, 104777.
- Rashby S. E., Sessions A. L., Summons R. E. and Newman D. K. (2007) Biosynthesis of 2-methylbacteriohopanepolyols by an anoxygenic phototroph. *Proc. Natl. Acad. Sci.* **104**, 15099–15104.
- Reghizzi M., Lugli S., Manzi V., Rossi F. and Roveri M. (2018) Orbitally Forced Hydrological Balance During the Messinian Salinity Crisis: Insights From Strontium Isotopes (Sr-87/Sr-86) in the Vena del Gesso Basin (Northern Apennines, Italy). *Paleoceanogr. Paleoclimatology* **33**, 716–731.

- Rouchy J. and Caruso A. (2006) The Messinian salinity crisis in the Mediterranean basin: A reassessment of the data and an integrated scenario. *Sediment. Geol.* **188**, 35–67.
- Rouchy J. M. and Blanc-Valleron M.-M. (2006) *Les Evaporites - Matériaux singuliers, milieux extrêmes*. Vuibert., Société Géologique de France.
- Roveri M., Flecker R., Krijgsman W., Lofi J., Lugli S., Manzi V., Sierro F., Bertini A., Carnerlenghi A., De Lange G., Govers R., Hilgen F., Hubscher C., Meijer P. and Stoica M. (2014) The Messinian Salinity Crisis: Past and future of a great challenge for marine sciences. *Mar. Geol.* **352**, 25–58.
- Roveri M., Gennari R., Ligi M., Lugli S., Manzi V. and Reghizzi M. (2019) The synthetic seismic expression of the Messinian salinity crisis from onshore records: Implications for shallow- to deep-water correlations. *Basin Res.*, 1121–1152.
- Ryan W. (2009) Decoding the Mediterranean salinity crisis. *Sedimentology* **56**, 95–136.
- Sanford W. E. and Wood W. W. (1991) Brine evolution and mineral deposition in hydrologically open evaporite basins. *Am. J. Sci.* **291**, 687–710.
- Sayama M., Risgaard-Petersen N., Nielsen L. P., Fossing H. and Christensen P. B. (2005) Impact of bacterial NO_3^- transport on sediment biogeochemistry. *Appl Env. Microbiol* **71**, 7575–7577.
- Schmaljohann R., Drews M., Walter S., Linke P., von Rad U. and Imhoff J. F. (2001) Oxygen-minimum zone sediments in the northeastern Arabian Sea off Pakistan: a habitat for the bacterium *Thioploca*. *Mar. Ecol. Prog. Ser.* **211**, 27–42.
- Schoell M., Hwang R. J., Carlson R. M. K. and Welton J. E. (1994) Carbon isotopic composition of individual biomarkers in gilsonites (Utah). *Org. Geochem.* **21**, 673–683.
- Schopf J. W., Farmer J. D., Foster I. S., Kudryavtsev A. B., Gallardo V. A. and Espinoza C. (2012) Gypsum-permineralized microfossils and their relevance to the search for life on Mars. *Astrobiology* **12**, 619–33.
- Schulz H. N. and Jorgensen B. B. (2001) Big bacteria. *Annu. Rev. Microbiol.* **55**, 105–137.
- Schutte C. A., Teske A., MacGregor B. J., Salman-Carvalho V., Lavik G., Hach P. and de Beer D. (2018) Filamentous Giant *Beggiatoaceae* from the Guaymas Basin Are Capable of both Denitrification and Dissimilatory Nitrate Reduction to Ammonium ed. I. Cann. *Appl. Environ. Microbiol.* **84**, e02860-17.
- Seitaj D., Schauer R., Sulu-Gambari F., Hidalgo-Martinez S., Malkin S. Y., Burdorf L. D. W., Slomp C. P. and Meysman F. J. R. (2015) Cable bacteria generate a firewall against euxinia in seasonally hypoxic basins. *Proc. Natl. Acad. Sci.* **112**, 13278–13283.
- Shields G. A. and Mills B. J. W. (2020) Evaporite weathering and deposition as a long-term climate forcing mechanism. *Geology* **49**, 299–303.

Sim M. S., Bosak T. and Ono S. (2011) Large Sulfur Isotope Fractionation Does Not Require Disproportionation. *Science* **333**, 74–77.

Sinninghe Damsté J. P., Frewin N. L., Keing F. and De Leeuw J. W. (1995) Molecular indicators for palaeoenvironmental change in a Messinian evaporitic sequence (Vena del Gesso, Italy). I: Variations in extractable organic matter of ten cyclically deposited marl beds. *Org. Geochem.* **23**, 471–483.

Sofer Z. (1978) Isotopic composition of hydration water in gypsum. *Geochim. Cosmochim. Acta* **42**, 1141–1149.

Sofer Z. and Gat J. R. (1972) Activities and concentrations of oxygen-18 in concentrated aqueous salt solutions: analytical and geophysical implications. *Earth Planetary Sci. Lett.* **15**, 232–238.

Sofer Z. and Gat J. R. (1975) The isotope coposition of evaporating brines: effect of the isotopic activity ratio in saline solutions. *Earth Planet. Sci. Lett.* **26**, 179–186.

Sommer S., Gier J., Treude T., Lomnitz U., Dengler M., Cardich J. and Dale A. W. (2016) Depletion of oxygen, nitrate and nitrite in the Peruvian oxygen minimum zone cause an imbalance of benthic nitrogen fluxes. *Deep Sea Res. Part Oceanogr. Res. Pap.* **112**, 113–122.

Spencer R. J. and Hardie L. A. (1990) Control of Seawater composition by mixing of river waters and mid-ocean ridge hydrothermal brines. In *Fluid-Mineral Interactions: A Tribute to H.P. Eugster* Special Publication. The Geochemical Society. pp. 409–419.

Stewart F. H. (1963) *Marine Evaporites.*, U.S. Geological Survey.

Stumm W. and Morgan J. J. (1996) *Aquatic Chemistry: Chemical Equilibria and Rates in Natural Waters*. 3rd ed., John Wiley & Sons, New York.

Tenhaven H. L. (1989) Tetrahymanol, the most likely precursor of gammacerane, occurs ubiquitously in marine sediments. *Geochim. Cosmochim. Acta* **53**, 3073–3079.

Teske A. and Nelson D. C. (2006) The Genera *Beggiatoa* and *Thioploca*. In *The Prokaryotes* (eds. M. Dworkin, S. Falkow, E. Rosenberg, K.-H. Schleifer, and E. Stackebrandt). Springer New York, New York, NY. pp. 784–810.

Testa G. and Lugli S. (2000) Gypsum–anhydrite transformations in Messinian evaporites of central Tuscany (Italy). *Sediment. Geol.* **130**, 249–268.

Thamdrup B., Finster K., Fossing H., Hansen J. and Jorgensen B. (1994) Thiosulfate and Sulfite Distributions in Porewater of Marine-Sediments Related to Manganese, Iron, and Sulfur Geochemistry. *Geochim. Cosmochim. Acta* **58**, 67–73.

Thode H. G. and Monter J. (1965) Sulfur-Isotope Geochemistry of Petroleum, Evaporites, and Ancient Seas. In *Fluids in Subsurface Environments* American Association of Petroleum Geologists.

- Thode H., Monster J. and Dunford H. (1961) Sulphur Isotope Geochemistry. *Geochim. Cosmochim. Acta* **25**, 159–174.
- Topper R., Flecker R., Meijer P. and Wortel M. (2011) A box model of the Late Miocene Mediterranean Sea: Implications from combined Sr-87/Sr-86 and salinity data. *Paleoceanography* **26**.
- Topper R., Lugli S., Manzi V., Roveri M. and Meijer P. (2014) Precessional control of Sr ratios in marginal basins during the Messinian Salinity Crisis? *Geochem. Geophys. Geosystems* **15**, 1926–1944.
- Turchyn A. V., Bruchert V., Lyons T. W., Engel G. S., Balci N., Schrag D. P. and Brunner B. (2010) Kinetic oxygen isotope effects during dissimilatory sulfate reduction: A combined theoretical and experimental approach. *Geochim. Cosmochim. Acta* **74**, 2011–2024.
- Turchyn A. V. and De Paolo D. J. (2019) Seawater Chemistry Through Phanerozoic Time. *Annu. Rev. Earth Planet. Sci.* **47**, 197–224.
- Turchyn A. V. and Schrag D. P. (2004) Oxygen Isotope Constraints on the Sulfur Cycle over the Past 10 Million Years. *Science* **303**, 2004–2007.
- Usiglio J. (1849) Analyse de l'eau de la Méditerranée sur les côtes de France. *Ann. Chim.* **27**, 92–107, 172–191.
- Utrilla R., Pierre C., Ortí F. and Pueyo J. J. (1992) Oxygen and sulphur isotope compositions as indicators of the origin of Mesozoic and Cenozoic evaporites from Spain. *Chem. Geol.* **102**, 229–244.
- Vai G. B. and Ricci Lucchi F. (2006) Algal crusts, autochthonous and clastic gypsum in a cannibalistic evaporite basin: a case history from the Messinian of northern Apennines. *Sedimentology* **24**, 211–244.
- Valyashko M. G. (1972) Playa lakes - a necessary stage in the development of a salt-bearing basin. In *Geology of Saline Deposits* (ed. G. Richter-Bernburg). UNESCO, Paris. pp. 41–52.
- Van Driessche A. E. S., Canals A., Ossorio M., Reyes R. C. and García-Ruiz J. M. (2016) Unraveling the Sulfate Sources of (Giant) Gypsum Crystals Using Gypsum Isotope Fractionation Factors. *J. Geol.* **124**, 235–245.
- Van't Hoff J. H. (1912) *Untersuchungen über die Bildungsverhältnisse der ozeanischen Salzablagerungen.*, Leipzig.
- de la Vara A., van Baak C., Marzocchi A., Grothe A. and Meijer P. (2016) Quantitative analysis of Paratethys sea level change during the Messinian Salinity Crisis. *Mar. Geol.* **379**, 39–51.
- Vasiliev I., Karakitsios V., Bouloubassi I., Agiadi K., Kontakiotis G., Antonarakou A., Triantaphyllou M., Gogou A., Kafousia N., de Rafelis M., Zarkogiannis S., Kaczmar F.,

Parinos C. and Pasadakis N. (2019) Large Sea Surface Temperature, Salinity, and Productivity-Preservation Changes Preceding the Onset of the Messinian Salinity Crisis in the Eastern Mediterranean Sea. *Paleoceanogr. Paleoclimatology* **34**, 182–202.

Wakeham S. G., Amann R., Freeman K. H., Hopmans E. C., Jørgensen B. B., Putnam I. F., Schouten S., Sinninghe Damsté J. S., Talbot H. M. and Woebken D. (2007) Microbial ecology of the stratified water column of the Black Sea as revealed by a comprehensive biomarker study. *Org. Geochem.* **38**, 2070–2097.

Warren J. K. (2006) *Evaporites, Sediments, Resources and Hydrocarbons.*, Springer.

Wortmann U. G., Chernyavsky B., Bernasconi S. M., Brunner B., Boettcher M. E. and Swart P. K. (2007) Oxygen isotope biogeochemistry of pore water sulfate in the deep biosphere: Dominance of isotope exchange reactions with ambient water during microbial sulfate reduction (ODP Site 1130). *Geochim. Cosmochim. Acta* **71**, 4221–4232.

Wortmann U. G. and Chernyavsky B. M. (2007) Effect of evaporite deposition on Early Cretaceous carbon and sulphur cycling. *Nature* **446**, 654–6.

Wortmann U. G. and Paytan A. (2012) Rapid variability of seawater chemistry over the past 130 million years. *Science* **337**, 334–336.

Zerkle A. L., Farquhar J., Johnston D. T., Cox R. P. and Canfield D. E. (2009) Fractionation of multiple sulfur isotopes during phototrophic oxidation of sulfide and elemental sulfur by a green sulfur bacterium. *Geochim. Cosmochim. Acta* **73**, 291–306.

Zharkov M. A. (1981) *History of Paleozoic Salt Accumulation.*, Springer, Berlin, Heidelberg, New York.

Zopfi J., Kjaer T., Nielsen L. P. and Jorgensen B. B. (2001) Ecology of Thioploca spp.: Nitrate and sulfur storage in relation to chemical microgradients and influence of Thioploca spp. on the sedimentary nitrogen cycle. *Appl. Environ. Microbiol.* **67**, 5530–5537.

Tables

Table 1 – Summary of crystal-bound water isotopic composition and fluid inclusion salinity of Primary Lower Gypsum and Upper Gypsum deposits

Basin	Section	Gypsum parent water						Fluid inclusion salinity			Reference	
		$\delta^{18}\text{O}_{\text{H}_2\text{O}}$ (‰ vs SMOW)			$\delta\text{D}_{\text{H}_2\text{O}}$ (‰ vs SMOW)							
		Min	Max	Av. (n ^b)	Min	Max	Av.	Min	Max	Av.(n ^b)		
Caltanissetta	EM	3.64	5.78	4.71 (31)	16.99	28.05	22.11	-	-	-	this work	
	SE	1.03	3.60	2.43 (14)	-1.51	13.88	5.36	-	-	-	this work	
	GI	-2.62	2.51	0.48 (6)	-22.44	13.78	-0.77	-	-	-	this work	
Vena del Gesso	Mo/MT	0.99	4.34	2.74 (35)	0.91	22.07	11.49	24.5	78.2	52.2 (6)	this work	
Piedmont	BA	0.28	3.15	1.76 (45)	1.61	23.48	11.86	2 ^a	77 ^a	16 ^a (7)	Natalicchio et al. (2014) and this work	
	AR	-3.47	2.38	-0.47 (27)	-31.96	17.59	-7.39	-	-	-	this work	
	PO	-7.00	2.48	-1.47 (72)	-56.43	10.64	-14.57	-	-	-	this work	
Sorbas	RA	-2.06	3.21	0.83 (25)	-17.04	15.03	-0.36	18.8	50.7	32.3 (11)	Evans et al. (2015)	
Catanzaro Trough	MQ	-	-	-	-	-	-	1.8	65 ^f	27 (24)	Costanzo et al. (2019)	
Modern salina	Cabo de Agua	6.3	7.6	7.42 (5)	29.6	38.62	33.13	-	-	-	Evans et al. (2015)	
	Cagliari	6.2	7.3	-	-	-	-	-	-	-	Longinelli (1979)	
	Aigues-Mortes	7.1 ^c	8.7 ^c	7.90 (8)	27.0	37.6	32.07	-	-	-	Fontes (1965) Fontes and Gonfiantini (1967)	
	Salin-de Giraud	4.5 ^d	6.4 ^d	5.13 (3)	18.9 ^d	29.5 ^d	22.50	-	-	-	Pierre (1982a)	
		3.7 ^e	4.6 ^e	4.03 (3)	12.4 ^e	17.4 ^e	14.30	-	-	-	Pierre (2018)	

Notes: EM-Eraclea Minoa; SE-Santa Elisabetta; GI-Gibliscemi; MT-Monte Tondo; BA-Banengo; AR-Arnulfi; PO-Pollenzo; RA-Rio de Aguas; MQ-Marcellinara Quarry; ^aFluid inclusion salinity was measured by Natalicchio et al (2014) on gypsum samples from the Banengo and Moncucco sections; ^bindicates the number of macroscopic gypsum samples investigated; ^cvalues reported by Pierre (1982); ^dmm-thick, seasonal gypsum crust sampled in July 1976; ^epluri-annual, cm-thick gypsum crusts subject to seasonal cycles of dissolution/ re-crystallisation by meteoric waters, sampled in March 1978; ^fdisregards one outlier salinity value at 115 g kg⁻¹.

Table 2 – Chemical and isotopic composition of the Mediterranean, Black and Caspian seas and of the major rivers that feed them.

	Water discharge (km ³ /yr)	[Sr ²⁺] (µM)	⁸⁷ Sr/ ⁸⁶ Sr (-)	[Ca ²⁺] (mM)	[SO ₄ ²⁻] (mM)	δ ³⁴ S _{SO4} vs CDT	References
<i>Mediterranean Sea rivers</i>							
Nile	83	2.68	0.706-0.7071	0.775	0.542	-	Brass (1976) Gerstenberger et al. (1997)
Rhone	54	5.94	0.7087	1.770	0.479	-	Gaillardet et al. (1999)
<i>Black Sea rivers</i>							
Danube	207	2.76	0.7089	1.473	0.660	7.6	Gaillardet et al. (1999) Burke et al. (2018)
Dniester	11	-	-	1.725	0.319	5.5	Burke et al. (2018)
Dnieper	54	2.5	0.7084	1.105	0.356	5.5	Gaillardet et al. (1999) Palmer and Edmond (1989) Burke et al. (2018)
Don	28.9	2.5	0.7084	2.073	0.953	5.8	Gaillardet et al. (1999) Palmer and Edmond (1989) Burke et al. (2018)
<i>Caspian Sea rivers</i>							
Volga	239.7	5.48	0.708083	1.1	0.67	7.4	Clauer et al. (2000) Kroonenberg et al. (2005) Mekhtieva and Rabinovich (1975)
Ural	8.8	-	-	-	-	5.2	Mekhtieva and Rabinovich (1975)
Western rivers	33.6	18.8	0.707795	-	-	-	Clauer et al. (2000)
Southern rivers	10.2	9.7	0.708293	-	-	-	Clauer et al. (2000)
<i>Water masses</i>							
Atlantic Ocean	-	87	0.709006	10.	28.9	22	McArthur et al. (2001) Berner and Berner (2012) Masterson et al. (2016)
Caspian Sea	-	114	0.708183	7,95	30	8.7	Clauer et al. (2000) Mekhtieva and Rabinovich (1975)

Notes: western Caspian rivers include Sulak, Samur, Kura and Terek

Table 3 – Mass balance estimate of the percentage of re-crystallized gypsum needed to explain gypsum parent water $\delta^{18}\text{O}$ values

Section	Messinian gypsum ^a		Meteoric H ₂ O	Pure evaporitic gypsum ^e	Recrystallized fraction	
	Min $\delta^{18}\text{O}$	Max $\delta^{18}\text{O}$	$\delta^{18}\text{O}$	$\delta^{18}\text{O}$	Max %	Min %
Eraclea Minoa	7.14	9.28	-7.00 ^b	6.5	21.2	5.3
S. Elisabetta	4.53	7.10	-7.00 ^b	6.5	40.5	21.5
Gibliscemi	0.88	6.01	-7.00 ^b	6.5	67.6	29.6
Monte Tondo	0.99	4.34	-8.00 ^c	6.5	62.1	39.0
Banengo	3.78	6.65	-9.00 ^d	6.5	40.1	21.6
Arnulfí	0.03	5.88	-9.00 ^d	6.5	64.3	26.6
Pollenzo	-3.50	5.98	-9.00 ^d	6.5	87.1	25.9
Sorbas	1.44	6.71	-5.11 ^d	6.5	73.7	28.3

Notes : ^aoxygen isotope composition of gypsum crystallization water; ^bLiotta et al. (2013);

^cGiustini et al. (2016); ^dEvans et al. (2016); ^eaverage $\delta^{18}\text{O}$ of the crystallization water of gypsum precipitated by evaporation of Mediterranean waters under summer (July) evaporative conditions (see Fig. 2f for corresponding water isotope composition).

Table 4 – Yearly cycle of hydrological and biogeochemical processes that lead to the formation of one mm-thick gypsum lamina in marginal basins

Precession	Season	Reservoir	Process
Minimum precession = humidity	Humid and arid	Surface	Stratification decreases the transport of nutrients from deep water layer to surface layer, NO ₃ -based PP stops
			N ₂ -based primary production until P depletion, then oligotrophic surface layer (process 1): $106CO_2 + 16N_2 + H_3PO_4 + 154H_2O \rightarrow (CH_2O)_{106}(NH_3)_{16}(H_3PO_4) + 130O_2 + 16NH_3$
		Deep	At the oxic-anoxic interface, anoxygenic phototrophic bacteria oxidise H ₂ S to SO ₄ ²⁻ (process 2): $H_2S + 2CO_2 + 2H_2O \rightarrow 2CH_2O + SO_4^{2-} + 2H^+$
		Mat	Stratification decreases O ₂ transport to deep water layer
			O ₂ , consumed, NO ₃ ⁻ and PO ₄ ³⁻ build-up; eventually layer becomes anoxic (process 3): $(CH_2O)_{106}(NH_3)_{16}(H_3PO_4) + 138O_2 \rightarrow 106CO_2 + 16HNO_3 + H_3PO_4 + 122H_2O$
		Arid	when deep water layer is anoxic, NO ₃ pumped into mat by Thioploca and reacts with H ₂ S to form S° (process 4: DNRA): $HS^- + 0.25NO_3^- + 1.5CO_2 + 0.75H_2O \rightarrow S^\circ + 0.25NH_4^+ + 1.5HCO_3^-$
			Sulfate reduction produces H ₂ S (process 5): $(CH_2O)_{106}(NH_3)_{16}(H_3PO_4) + 53SO_4^{2-} \rightarrow 67HCO_3^- + 53HS^- + 122H_2O$
	Arid	Surface	Convection mixes deep water nutrients into surface water layer
			NO ₃ -based primary production and export to deep layer (process 6): $106CO_2 + 16HNO_3 + H_3PO_4 + 122H_2O \rightarrow (CH_2O)_{106}(NH_3)_{16}(H_3PO_4) + 138O_2$
		Deep	Convection mixes surface water oxygen into deep water layer
			Aerobic degradation of exported C-org (process 7): $(CH_2O)_{106}(NH_3)_{16}(H_3PO_4) + 138O_2 \rightarrow 106CO_2 + 16HNO_3 + H_3PO_4 + 122H_2O$
		Mat	Planktic CaCO ₃ particles dissolve in mat, releasing Ca ²⁺ (process 8): $CaCO_3 \rightarrow Ca^{2+} + CO_3^{2-}$
			Bottom water O ₂ pumped by Thioploca into mat from bottom waters, reacts with mat S° producing SO ₄ peak (process 9): $S^\circ + 1.5O_2 + 2HCO_3^- \rightarrow SO_4^{2-} + 2CO_2 + H_2O$
		All	Seasonal mm-thick gypsum layer precipitates (process 10): $Ca^{2+} + SO_4^{2-} \rightarrow CaSO_4$
	Humid	All	Same stratified conditions as during minimum precession

Figure captions

Figure 1 – Marginal basin gypsum deposits formed during the Messinian salinity crisis. (a) Map of Mediterranean Sea showing the modern distribution of offshore and onshore deposits related to the Messinian Salinity Crisis. The geographical location of marginal basins (Sorbas, Piedmont, Vena del Gesso, Caltanissetta, Polemi and Mesaoria basins and the Catanzaro Trough) is shown, as well as the location of the Vaccarès Lagoon (Camargue Area, south of France), located 25 km away from the Aigues Mortes salt works; (b) Stratigraphic sections investigated in the present work.

Figure 2 – Geochemical evidence for the existence of low-salinity evaporitic gypsum deposits in the Mediterranean Sea. Vertical bars in panel (a) represent the frequency (left vertical axis) of salinity measurements made in primary fluid inclusion from gypsum from the Piedmont and Vena del Gesso basins (northern Italy) (this work), the Catanzaro Trough (Calabria, Southern Italy) (Costanzo et al., 2019) and the Sorbas basin (Evans et al., 2015); blue circles represent the salinity- $\delta^{18}\text{O}$ composition of Sorbas basin gypsum fluid inclusions (Evans et al., 2015). Coloured circles in panels (b) to (e) are the isotope composition ($\delta^{18}\text{O}_{\text{H}_2\text{O}}$ and $\delta\text{D}_{\text{H}_2\text{O}}$) of gypsum parent waters from the Caltanissetta (Sicily, Italy), Vena del Gesso (Apennines, Italy), Piedmont (Italy) (this work) and Sorbas (Spain) (Evans et al., 2015). Crosses, and the vertical grey band in panel f, indicate the isotope composition of parent waters of gypsum formed in modern salt works of the Mediterranean region (Fontes, 1966; Fontes and Gonfiantini, 1967; Longinelli, 1979; Evans et al., 2015). The black dot is the isotope composition of surface Atlantic water in front of Gibraltar (Benetti et al., 2017a). The continuous green line, followed by the green dotted line in panels (b) to (f), represent the model evolution in the $\delta^{18}\text{O}_{\text{H}_2\text{O}}-\delta\text{D}_{\text{H}_2\text{O}}$ space during the evaporation of Mediterranean Sea water under evaporative conditions based on *in-situ* atmospheric measurements from the Vaccarès Lagoon (Camargue area, southern France) (Delattre et al., 2015). The green dot with a black circle separating the continuous green line from the green dotted line represents the gypsum saturation point; the $\delta^{18}\text{O}_{\text{H}_2\text{O}}-\delta\text{D}_{\text{H}_2\text{O}}$ evolution after the gypsum saturation point (green dotted line) reflects the increasing importance of fractionation between free water molecules and water molecules within the hydration sphere of dissolved ions (Sofer and Gat, 1972, 1975). Note: MWL – Meteoric Water Line (Craig and Gordon, 1965).

Figure 3 – Sulfur ($\delta^{34}\text{S}$) and oxygen ($\delta^{18}\text{O}$) isotope composition of the dissolved sulfate ion deduced from the analyses of Primary Lower Gypsum and Upper Gypsum gypsum deposits

taking into account the sulfur (Thode and Monster, 1965) and oxygen (Lloyd, 1966) isotope fractionations between the dissolved sulfate ion and gypsum ($\varepsilon^{34}\text{S}_{\text{SO}_4-\text{GYP}} = -1.65 \text{ ‰}$ and $\varepsilon^{18}\text{O}_{\text{SO}_4-\text{GYP}} = -3.6 \text{ ‰}$, respectively). Previously published Primary Lower Gypsum data (Lu et al., 2001; Evans et al., 2015; Garcia-Veigas et al., 2020) has been corrected, where, appropriate, taking into account the latest reported values of $\delta^{34}\text{S}$ and $\delta^{18}\text{O}$ of the NBS 127 barium sulfate standard (Brand et al., 2014). Data from Mesozoic and Cenozoic gypsum deposits from southern Spain (“ancient gypsum > 14 Ma”) was taken from Utrilla et al. (1992).

Figure 4 – Modelled co-evolution of: (a) salinity and $\delta^{18}\text{O}_{\text{H}_2\text{O}}$, and (b) salinity and gypsum saturation state (Ω_{gypsum}) of mixtures of Atlantic water and continental runoff subject to evaporation with different evaporative conditions (salt-works versus Mediterranean Sea) and runoff chemistry (ion-free runoff versus Ca^{2+} - and SO_4^{2-} -bearing runoff). In (a), model curves are compared to the fluid-inclusion salinity and $\delta^{18}\text{O}_{\text{H}_2\text{O}}$ of parent waters of gypsum deposits from Primary Lower Gypsum cycle 6 from the Sorbas basin (blue circles) (Evans et al., 2015). Notes: f_R is the fraction of continental runoff mixed with Atlantic ocean waters; evaporative conditions for the salt works scenario are based on atmospheric measurements at the Vaccarès Lagoon site (Camargue area, southern France; Delattre et al., 2015); green arrows in panel (b) show the average salinity of fluid inclusions in the Piedmont basin (PB) (Natalicchio et al., 2014), the Catanzaro Trough (CT) (Costanzo et al., 2019), the Sorbas basin (SB) (Evans et al., 2014) and the Vena del Gesso basin (VdG) (this work).

Figure 5 - $\delta^{34}\text{S}_{\text{SO}_4}$ composition of the dissolved sulfate ion in equilibrium with Primary Lower Gypsum and Upper Gypsum deposits formed in the marginal basins of the Mediterranean during the Messinian Salinity Crisis. Red crosses are the average $\delta^{34}\text{S}_{\text{SO}_4}$ values for given marginal basins (gray boxes) and for all the complete Primary Lower Gypsum and Upper Gypsum datasets (orange box, $n = 281$ for Primary Lower Gypsum and $n=94$ for Upper Gypsum). The lower and upper bounds of the boxes correspond to the 1st and 3rd quartile; the horizontal line inside the boxes represents the median; vertical lines (whiskers) extend to minimum and maximum values, excluding outliers (represented as small circles). The $\delta^{34}\text{S}_{\text{SO}_4}$ value from the Messinian ocean (22 ‰ vs CDT) is taken from Masterson et al. (2016). Data sources are: Piedmont basin (this work, Supplementary Tables 6,7,8); Caltanissetta basin (this work, Supplementary Tables 2,3,4; Garcia-Veigas et al., 2018); Sorbas basin (Playa et al., 2000; Evans et al., 2015; Garcia-Veigas et al., 2018); Nijar basin (Lu et al., 2001); Vena

del Gesso (Supplementary Table 5 and (Lugli et al., 2007); Mallorca (Garcia-Veigas et al., 2018); Feos (Lu et al., 2001); Polemi basin (Pierre, 1982).

Figure 6 – Modelled salinity and isotope composition ($\delta^{34}\text{S}_{\text{SO}_4}$ and $^{87}\text{Sr}/^{86}\text{Sr}$) of gypsum deposits precipitating from a mixture of seawater and river water with variable dissolved Ca^{2+} and SO_4^{2-} concentration (panels a,c and e) and Sr^{2+} concentrations and $^{87}\text{Sr}/^{86}\text{Sr}$ ratios (panels b, d and f). The graphs are drawn for a fraction of river water in the mixture equal to 0.9 (panels a and b), 0.6 (panels c and d) and 0.4 (panels e and f). In panels a, c and e, red contours represent the calculated salinity at gypsum saturation while the blue shaded area represents the range of salinities measured from fluid inclusions in gypsum from the Primary Lower Gypsum and Upper Gypsum units (Natalicchio et al., 2014; Evans et al., 2015; Costanzo et al., 2019); horizontal dotted lines represent the calculated $\delta^{34}\text{S}$ of dissolved SO_4^{2-} while the vertical orange and green bars represent the $\delta^{34}\text{S}$ of dissolved SO_4^{2-} deduced form isotope measurements of Primary Lower Gypsum and Upper Gypsum deposits (see text for references); the red dotted area represents the range of modern dissolved Ca^{2+} and SO_4^{2-} in the main rivers entering the Mediterranean, Black and Caspian seas (Table 2), while the red dot corresponds to the dissolved Ca^{2+} and SO_4^{2-} in the modern Caspian Sea. In panels b, d and f, the blue contours represent the calculated $^{87}\text{Sr}/^{86}\text{Sr}$ of dissolved Sr; the orange and light blue shaded areas represent the $^{87}\text{Sr}/^{86}\text{Sr}$ range of gypsum from the Primary Lower Gypsum and Upper Gypsum units, respectively (see text for references); the red dots represent the Sr flux-weighted dissolved Sr concentration and $^{87}\text{Sr}/^{86}\text{Sr}$ ratio of runoff considering only the Nile and the Rhone rivers (Nile/Rhone), only rivers draining into the modern Black ad Caspian seas (BS/CS rivers), and all of these sources (All rivers).

Figure 7 – (a), (b) Transmitted light photomicrographs of twinned selenite crystals from the 2nd cycle of the Primary Lower Gypsum unit (Banengo section, Piedmont basin (a)) and the 4th Primary Lower Gypsum cycle from the Vena del Gesso Basin (Monte Tondo section, (b)). An internal lamination, given by the alternation of turbid and limpid laminae is recognizable in the re-entrant angle of both the crystals Note how the crystal shape is perfectly preserved and no evidence of diagenetic alteration is visible. The dotted rectangle in panel A indicate the location of panel (c). (c) Detail of (a) showing the lamination in the re-entrant angle of the twin. Turbid laminae (T) rich in filamentous microfossils alternate with more limpid laminae (L) in which the latter are scarce. (d) UV light photomicrograph of filaments (white arrows) from the Vena del Gesso Basin (Monte Tondo section, 4th Primary Lower Gypsum cycle). Note the high autofluorescence of the filament and the tiny opaque iron sulfide grains,

corresponding to the product of diagenetic transformation of original sulfur globules. (e) UV light photomicrograph of an organic rich marine snow floccules entrapped in a twinned selenite crystals from the Vena del Gesso basin (Monte Tondo section, 3rd Primary Lower Gypsum cycle).

Figure 8 – Scenario proposed in this work for the formation of low-salinity gypsum as a side-product of the biogeochemical sulfur cycle.

Declaration of interests

The authors declare that they have no known competing financial interests or personal relationships that could have appeared to influence the work reported in this paper.

The authors declare the following financial interests/personal relationships which may be considered as potential competing interests:

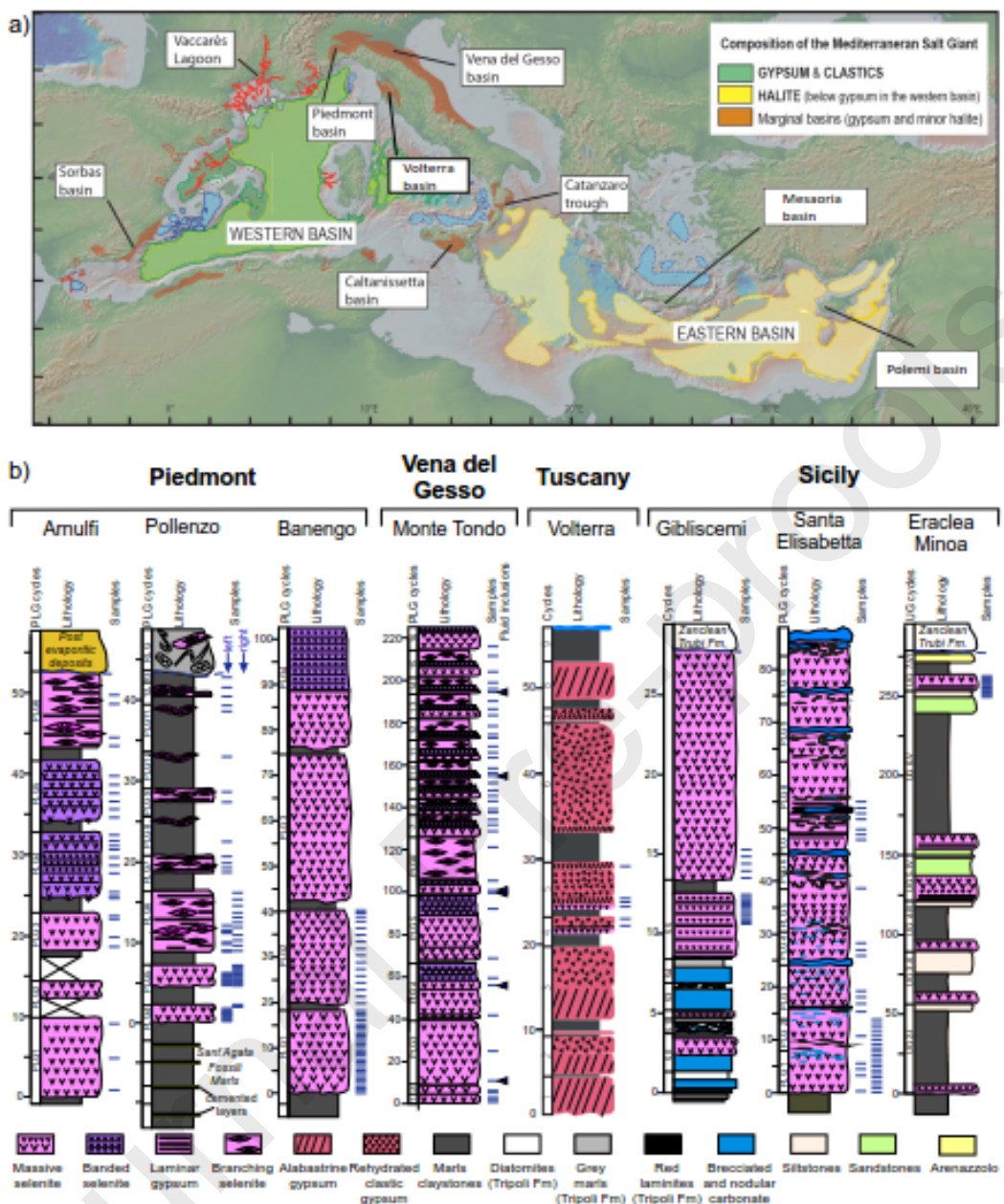


Figure 1

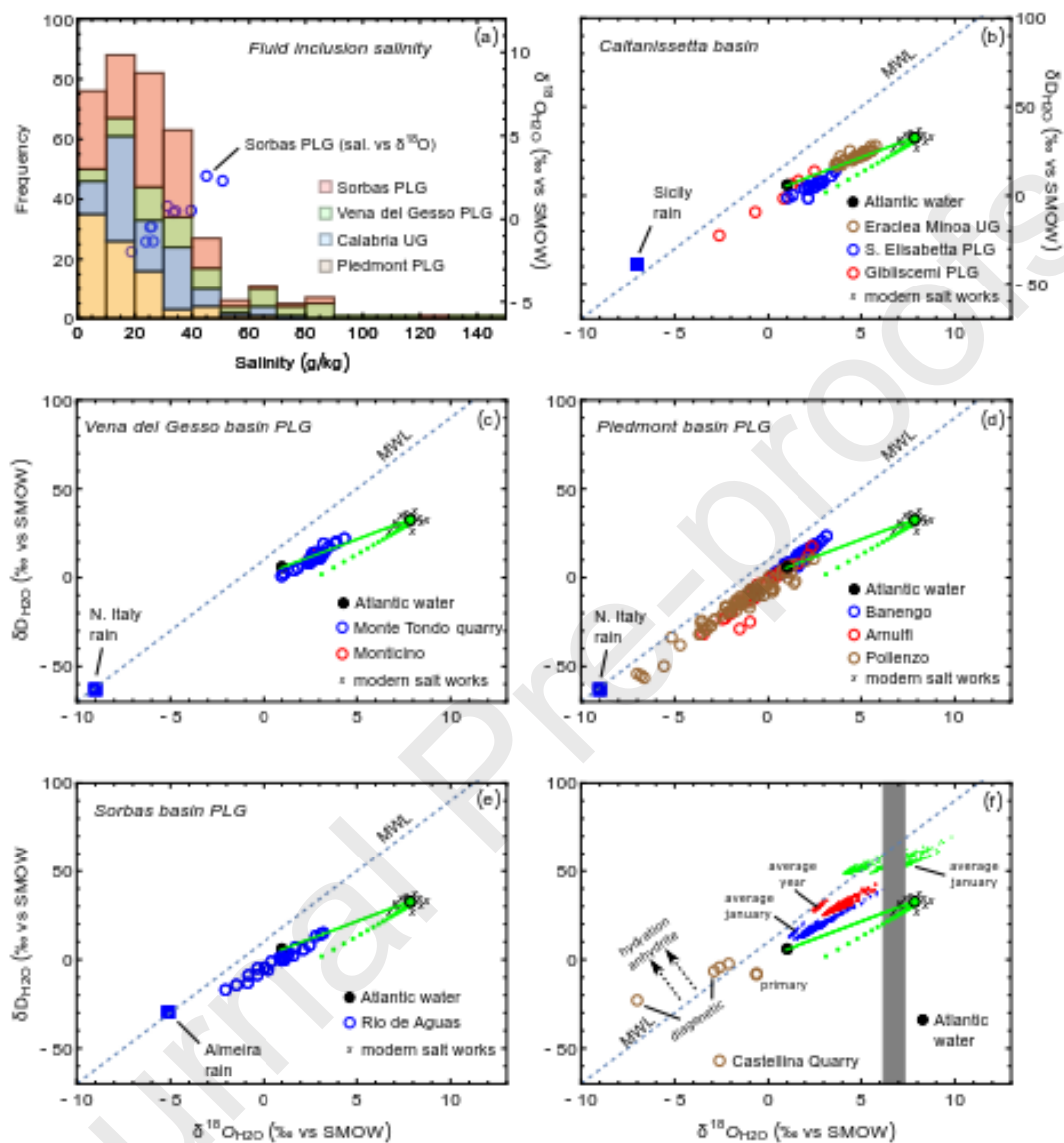


Figure 2

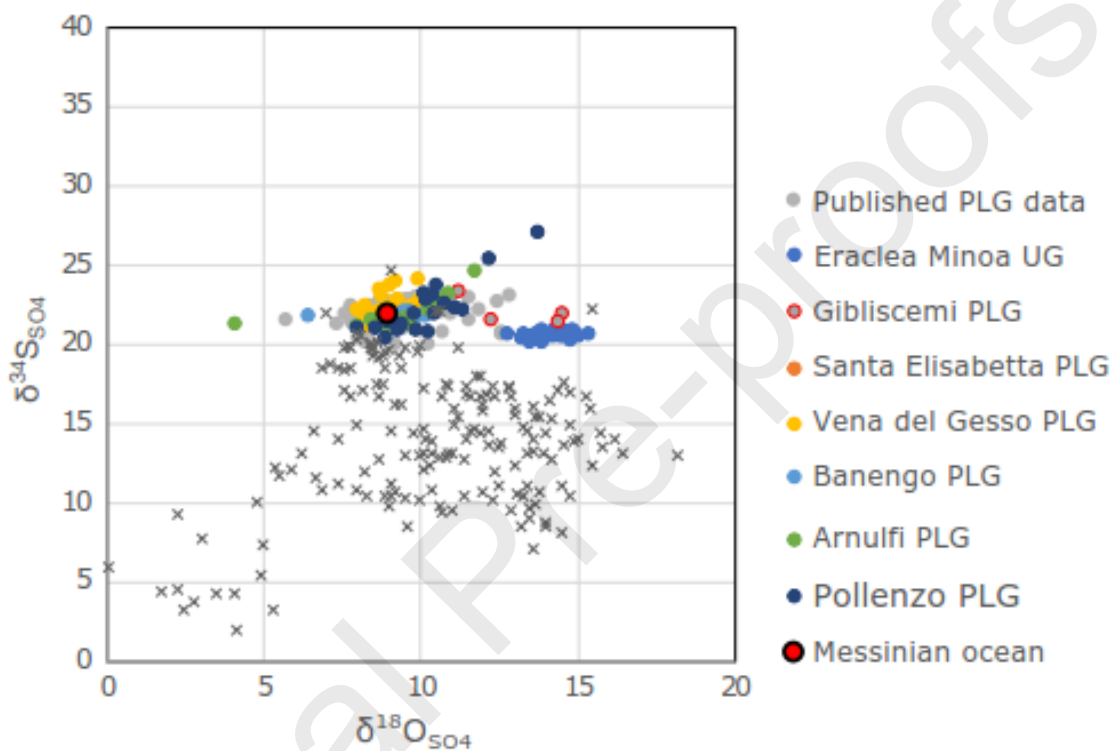


Figure 3

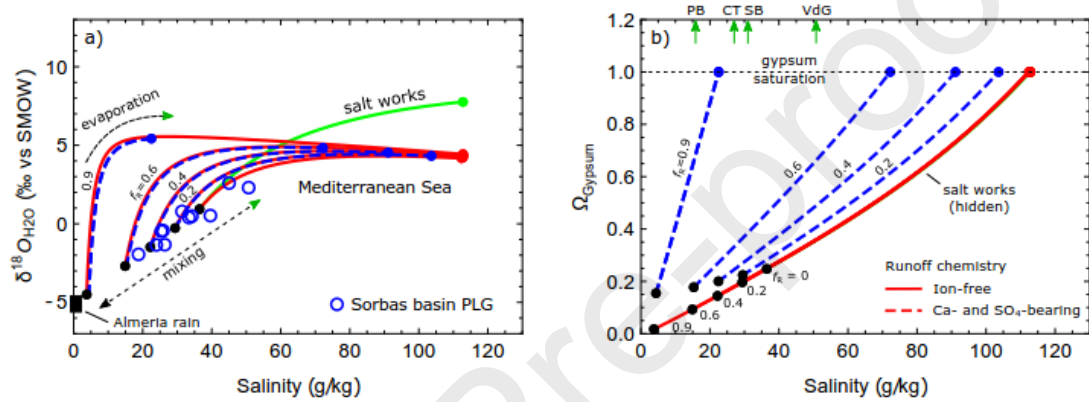


Figure 4

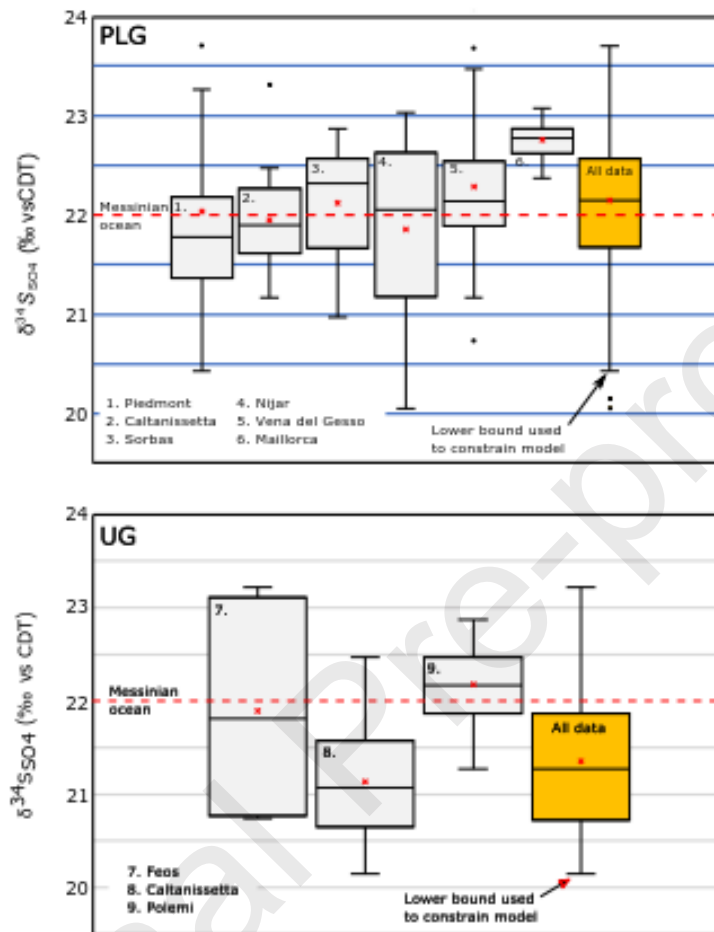


Figure 5

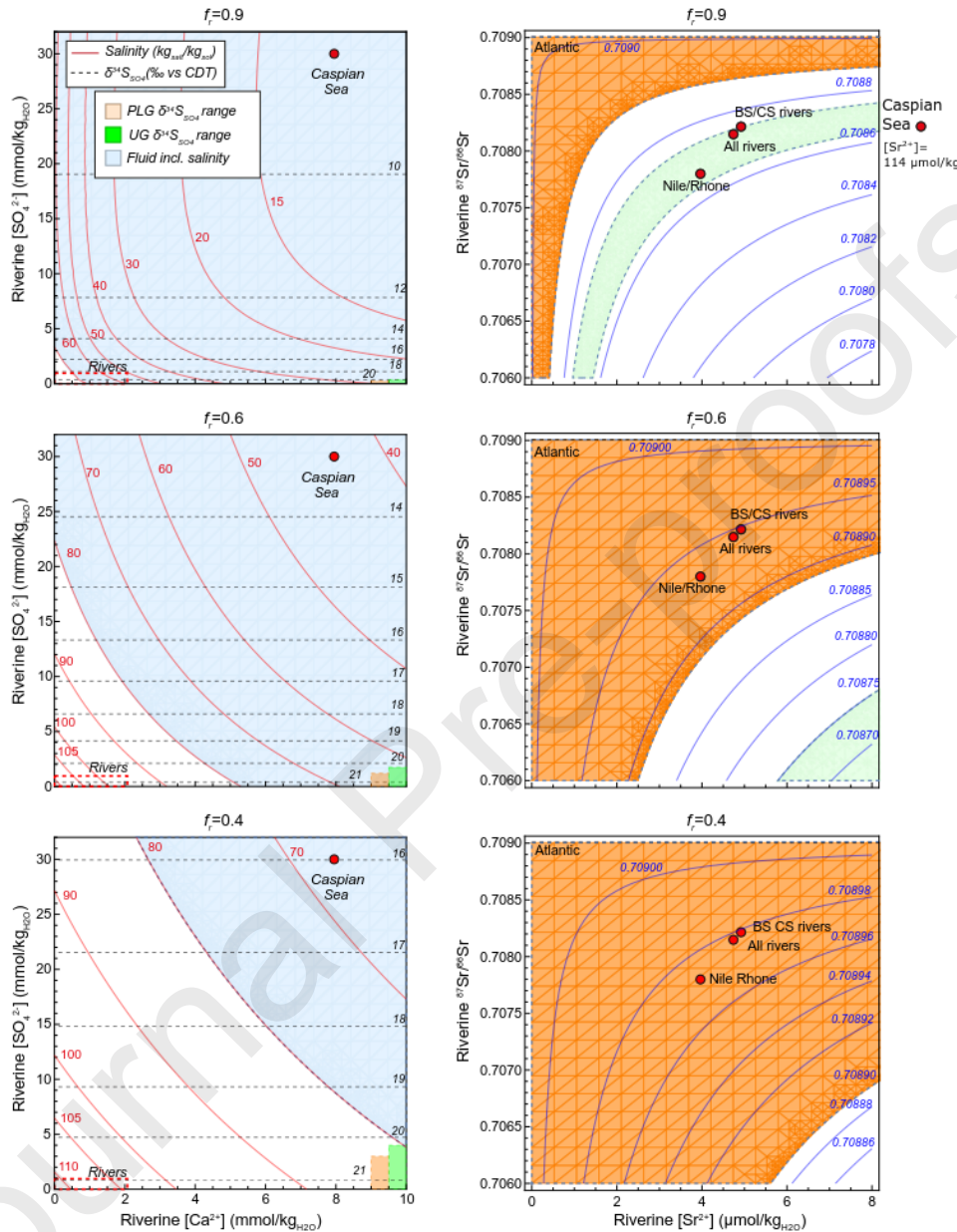


Figure 6

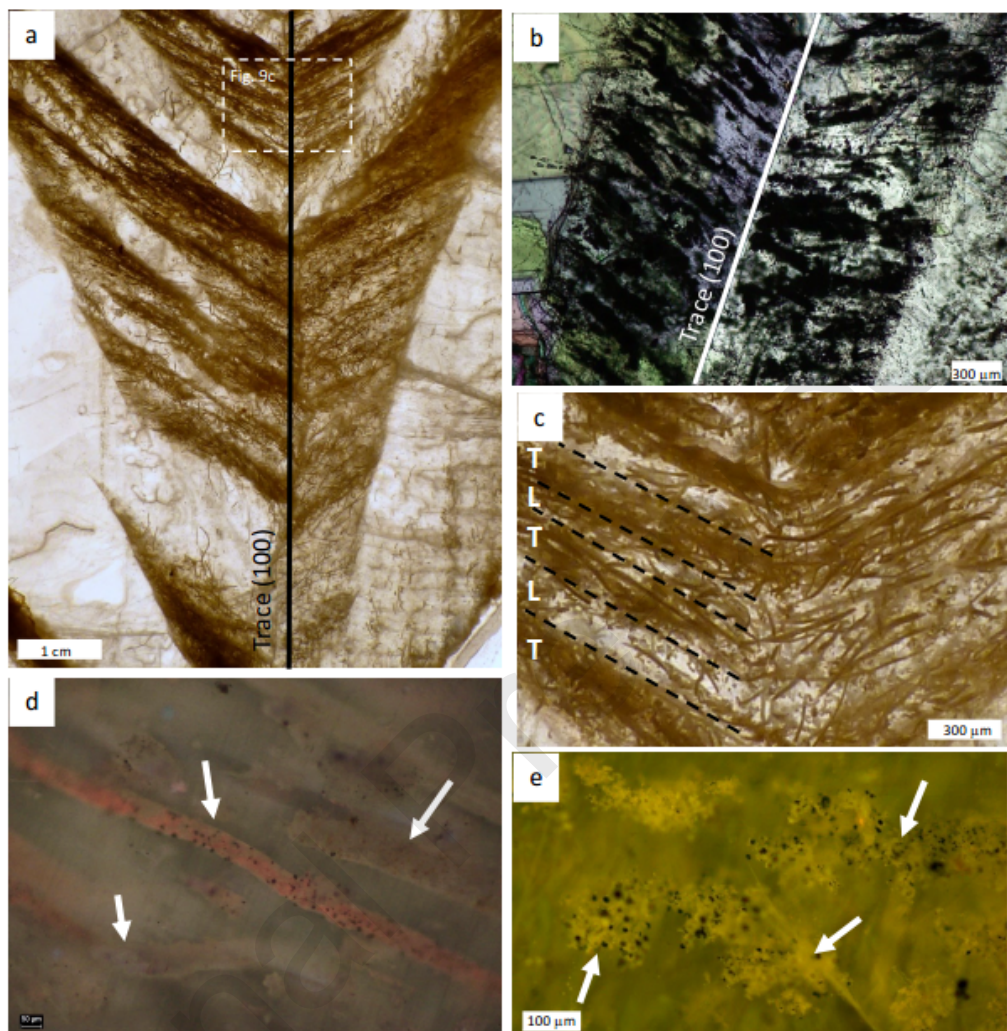


Figure 7

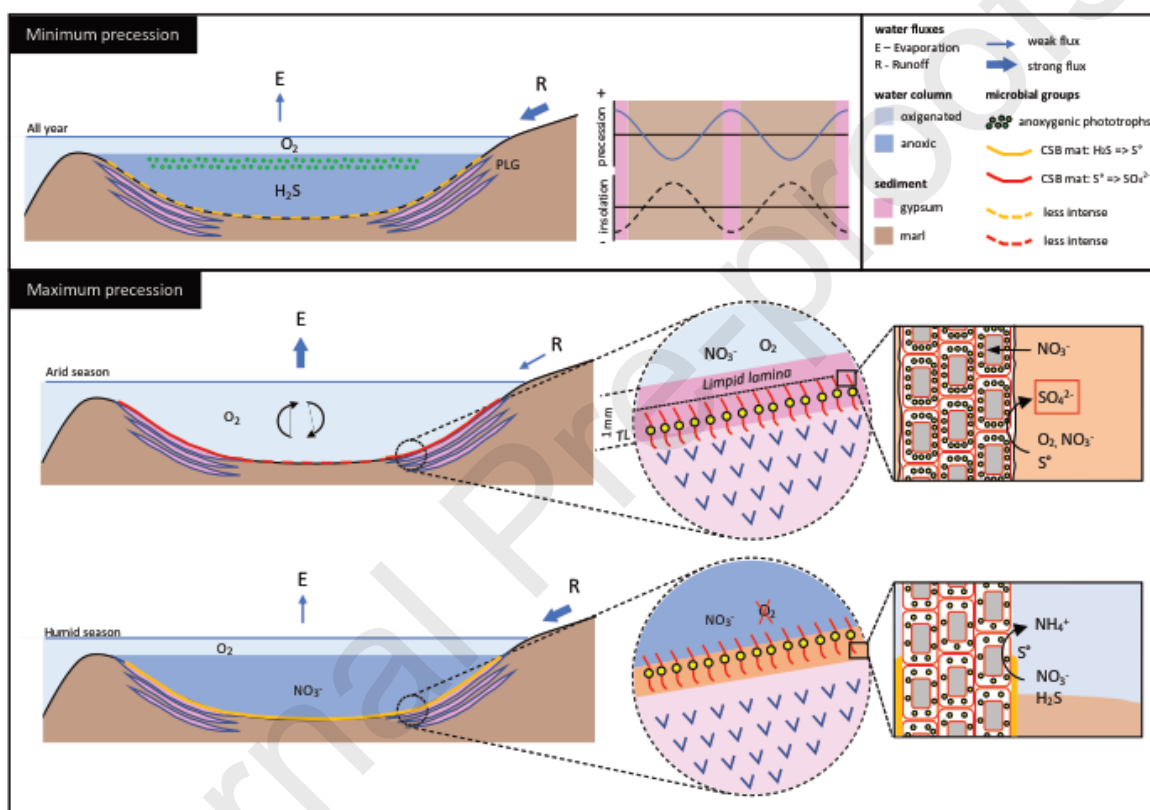


Figure 8